2007

Microwave Synthesis Of Nanocrystalline Hydroxy Apatite And Comparison Of Its Biomechanical Properties With Tio2 Structures

Saurabh Verma
University of Central Florida

MICROWAVE SYNTHESIS OF NANOCRYSTALLINE HYDROXYAPATITE AND COMPARISON OF ITS BIOMECHANICAL PROPERTIES WITH TiO_2 STRUCTURES

by

SAURABH VERMA
B.E. Punjab Engineering College, 2005

A thesis submitted in partial fulfillment of the requirements
for the degree of Master of Science
in the Department of Mechanical, Materials and Aerospace Engineering
in the College of Engineering and Computer Science
at the University of Central Florida
Orlando, Florida

Fall Term
2007

ABSTRACT

Nanocrystalline hydroxyapatite (HAp) powder of size 10-20 nm was synthesized applying microwave radiation using calcium nitrate tetrahydrate and sodium phosphate dibasic anhydrous as the starting materials. Microwave power of 600 W and Ca/P ratio of 1.66 in the starting chemicals served as the major factors in the synthesis of nanocrystalline HAp powder.

Phase composition and evolution were studied using X-ray diffraction (XRD) technique. Morphology, agglomeration and particle-size of the synthesized powder were studied using Scanning Electron Microscopy (SEM) and Transmission Electron Microscopy (TEM) techniques. Energy Dispersive Spectrum (EDS) was used to determine the elemental composition of the powder. Thermal properties were investigated using Thermogravimetric (TG) and Differential Thermal Analysis (DTA) and, Fourier Transform Infrared Spectroscopy (FTIR).

As-synthesized HAP and TiO_2 powder was uniaxially compacted into cylindrical pellets at a pressure of 78.69 MPa and sintered at high temperature to examine the effects of sintering on nano powder particles, densification behavior, phase evolution and mechanical properties. Phase evolution was studied using XRD whereas microstructure evolution was studied by SEM. To determine the mechanical properties Vickers hardness and biaxial flexural strength tests were performed.

Biodegradability and biomechanical strength of nano-HAp and TiO_2 samples sintered at high temperature was assessed in Simulated Body Fluid (SBF) having ionic concentration as that

of human plasma. Biodegradation and change in mechanical properties of the sintered samples when kept in SBF and maintained in a dynamic condition were studied in terms of weight loss, change in Vickers hardness and biaxial flexural strength as a function of time.

Highly crystalline HAp powder was achieved after microwave synthesis with average particle size in the range of 10-20 nm which was further confirmed by HR-TEM and SEM. Calcination of the synthesized powder at 500^{o}C for 2 h increased the average particle size to 21 nm. EDS confirmed the elemental composition of the powder. FTIR analysis showed the presence of phosphate band which confirmed the presence of HAp at high temperature. TG analysis showed 23% weight-loss upon heating up to 1200^{o}C, contributed by the removal of adsorbed & possible lattice water, decarboxylation of HAp or condensation of HPO_4^{2-} releasing water.

HAp along with β $NaCaPO_4$ and $Na_3Ca_6(PO_4)_5$ was observed at 950^{o}C, 1100^{o}C and 1200^{o}C. Density of HAp samples continued increasing with the increase in temperature from 1100^{o}C to 1250^{o}C and sintered density of 2.88 g/cc was obtained at 1250^{o}C.

Hardness and Biaxial strength of the HAp samples increased with temperature and maximum hardness value of 249.53 ± 3.98 HV and biaxial flexural strength of 52.07 ± 4.96 MPa were observed for samples sintered at 1250^{o}C.

Biaxial strength and hardness of TiO_2 samples increased with temperature. Maximum biaxial flexural strength of 125.5 ± 11.07 MPa and maximum hardness of 643.27 ± 7.96 HV were observed for the TiO_2 sample sintered at 1500^{o}C which was much more than that of sintered HAp samples.

Decrease in mass, hardness and biaxial strength of HAp samples sintered at 1250^{o}C and TiO_2 samples sintered at 1400^{o}C showed biodegradation in SBF, maintained in a dynamic state, as a function of time. Increase in mass was observed for the HAp samples in SBF during the fourth week.

Dedicated to my parents and friends

ACKNOWLEDGMENTS

I would like to express my gratitude to all those who helped me completing my M.S. degree requirements. I am deeply indebted to my advisor Dr Samar J. Kalita whose help, stimulating suggestions and encouragement motivated me during all phases of my research and in writing of this thesis. I would also like to express my sincere appreciation to Prof. Linan An and Prof. Helge Heinrich for being the committee members and evaluating my thesis. I also want to extend my thanks to Department of Mechanical, Materials and Aerospace Engineering (MMAE), Material Characterization Facility (MCF), Physical Plant of University of Central Florida (UCF) for financial and experimental support.

In addition, I would like to thank my colleagues and friends including Shipeng Qiu, Monica Hopkins, Andrew Warren, Prabhakar Mohan, Rene Diaz who provided useful hints and ideas throughout my research. Valuable assistance from Prof. Helge Heinrich and Prof. Sudipta Seal of Advanced Materials Processing and Analysis Center, UCF and, Dr. Nahid Mohajeri of Florida Solar Energy Center, Cocoa, FL, are of great significance in my final accomplishment and I would like to thank them all.

Finally, my most sincere thanks go to my beloved parents, for their everlasting and relentless love, support, encouragement and understanding.

TABLE OF CONTENTS

LIST OF FIGURES

LIST OF TABLES

LIST OF ACRONYMS/ABBREVATIONS

DTA	Differential thermal analysis
FTIR	Fourier Transform Infrared Spectroscopy
HAp	Hydroxyapatite
H-TEM	High Resolution Transmission Electron Microscopy
SEM	Scanning Electron Microscopy
TEM	Transmission Electron Microscopy
TG	Thermogravimetric
TiO_2	Titanium Dioxide
TTIP	Titanium Tetraisopropoxide
XRD	X-ray Diffraction

1. INTRODUCTION

1.1 Motivation

"The World Health Authority has decreed that 2000–2010 will be the Bone and Joint Decade, and this is now being supported by the United Nations [1]. The rationale for this is that joint diseases account for half of all chronic conditions for people over 65; back pain is the second leading cause of sick leave; and osteoporotic fractures have doubled in the last decade, so that 40% of all women over 50 will eventually suffer from one such fracture [1]. It is estimated that 25% of health expenditure in developing countries will be spent on trauma-related diagnostics by the end of the decade, and towards many children who are deprived of normal development due to crippling diseases and deformities"[1]

By 2020, half of the US population older than 50 will either have or will be in progress of developing osteoporosis or low bone mass. Every year about 1.5 million people suffer a bone fracture related to osteoporosis. Direct care cost for osteoporotic fractures is around $18 billion each year [2]. Osteoporosis and other bone diseases like osteosarcoma, osteogenesis imperfecta etc can lead to regress in physical health which may cause premature death too. Increasing aging population is the major factor which is running the orthopedic biomaterials market.

In 2002, the dental implants and dental bone substitutes market accounted for $296.5 million. Due to aging population, advances in technology, this market is supposed to touch $1 billion by 2011 [3]. The worldwide market for implant based dental reconstruction is believed to touch $ 3.5 billions by 2010 according to the study done by Kalorama Information.

Encompassing a vast gamut of technologies from simple wound dressing to sophisticated diagnostic equipment, the medical device market is having a rapid growth, the device ideas being mainly of academicians or clinicians. Then the devices are typically licensed on and sold by small companies. With the US market growing at an annual compound rate of 9%, some major characteristics like rapid innovation, more number of competitors with user friendly technologies etc. are helping the medical device industry grow fast. For a better understanding, the following comparisons can be looked at. [4]

Table 1: Geographical split of Worldwide Medical Devices Market [4]

Country	Market Size (2000) Billion (€)	% of World Market	Health Expenditure % GDP	Per capita Spend on Medical Devices (€)	Growth Rate (2000)
USA	60	37.5	13.9	125	7%
EU	41	25.6	5.7	66	5.5%
Japan	24.5	15.3	7.1	116	4%
Rest of the World	34.5	21.6	-	-	15%
Total	160	100	-	-	6%

Table 2: Key device market segments ranked by 2001 sales revenues [4]

Rank	Category	2001Sales (€ billion)
1	In vitro diagnostic devices	23.77
2	Minimally invasive surgery devices	19.02
3	Orthopedic devices	17.05
4	Wound care products	15.08
5	Cardiovascular devices	14.50
6	Ophthalmic devices	14.04

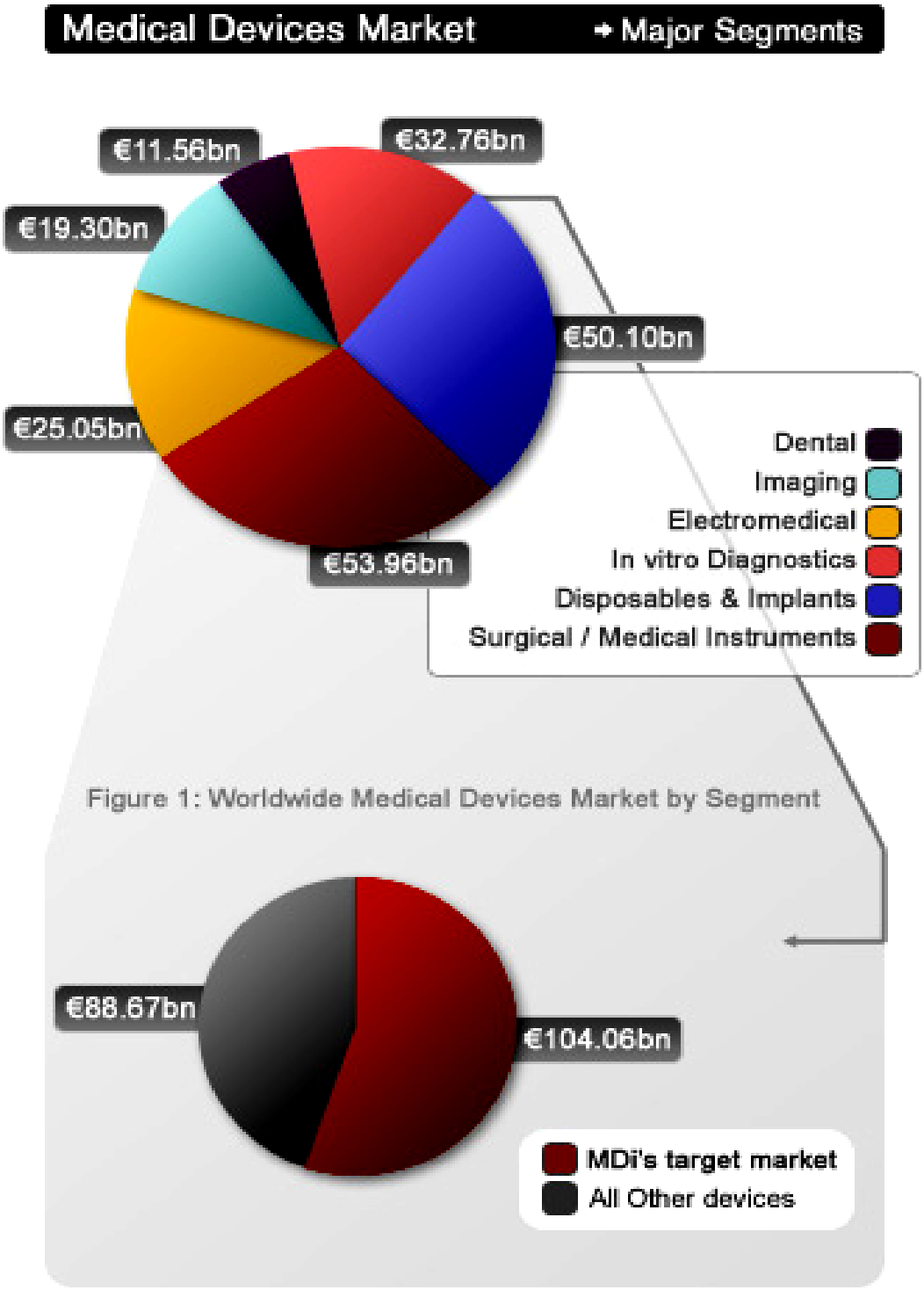

Figure 1: Graph showing the major segments in medical device market (2001-2002) [4]

My M.S. thesis research presents a single approach of synthesizing nanocrystalline HAp bioceramic powder using microwave radiation and comparison of the properties of sintered HAp structures with that of sintered TiO_2 structures prepared from nano-powder.

To treat, replace or repair amputated bone or tissue, various techniques like autografting (tissue graft within the same individual), allografting (tissue graft between two individuals of same species) and implantation of synthetic biomaterials which can be metallic, ceramic, polymer or composite have been developed. Limited number of donor sites and chronic donor sites pain limits the use of autografting technique. Success rate of autografting in old patients is much lower than the synthetic bone graft. In case of allograft, there is possibility of disease transmission and immunological response. Metallic biomaterials used in orthopedic have problem of stress shielding and subsequent weakening of host bone tissue which tend to implant failure. Bioceramics have compositional similarity with the bone mineral, so they can be preferable material for bone tissue engineering. Looking at the problems associated with autografting, allografting and metallic implant, there is great need to develop a novel ceramic which can be bonded with bone tissue and can help in cellular function and expression without any toxic response to the human body.

HAp is a material of choice for various biomedical applications like orthopedic, dentistry, drug delivery because of its similarity in composition to mineral phase of the bone, its excellent biocompatibility, its ability to promote cellular functions and expression and osteoconductivity. They elicit specific biological responses at the interface of the materials which result in the formation of strong bond between bone tissue and material.

On the other hand, titanium dioxide (TiO_2) ceramic has widely been used in the field of medical science because of its excellent biocompatibility as TiO_2 allows osseointegration between an artificial implant and bone. Properties and performance of TiO_2 depend strongly on particle size. Gleiter has shown that nanocrystalline ceramics offers improved mechanical, optical and electrical properties due to their high surface area to volume ratio [5]. Nano- TiO_2 can be synthesized using different techniques like Chemical Vapor Deposition (CVD), oxidation of Titanium Tetrachloride, thermal decomposition and Sol Gel technique. Poor mechanical strength of TiO_2 limits its use in structural applications like bone graft in bone tissue engineering. To improve its mechanical properties various investigation have been conducted. It has been proven that reduction in particle size is very effective in improving its mechanical strength [5]

1.2 Research objective

The primary objective of my MS research was to develop a simple and relatively high-speed process to synthesize nanocrystalline HAp bioceramic powder using microwave radiation which could easily be repeated. In addition, this research work investigated the densification behavior, sintering kinetics of the synthesized nanocrystalline HAp powder and evaluated mechanical performance and biodegradability of the sintered structures. Phases evolved at higher temperature were also analyzed for their bioactivity and resorbability in comparison to hydroxyapatite.

Another objective of this research was to compare the achieved mechanical properties of nano-structured HAp with structures made up of nanocrystalline TiO_2 powder. Synthesis of nano-TiO_2 powder was accomplished previously using a simple sol-gel process established by

Mr. Qiu Shipeng in our laboratory. Sintered TiO_2 samples were studied for their densification behavior and biaxial strength along with their biodegradability in Simulated Body Fluid with time.

The specific objectives of this research were as follows:

Objective 1: Synthesis of nano-HAp powder.

Objective 2: Characterization of the synthesized powder.

Objective 3: Sintering and densification study of nanocrystalline hydroxyapatite.

Objective 4: Assessment of Mechanical Properties of Sintered samples.

Objective 5: Assessment of Biomechanical Properties and Biodegradation in SBF.

1.3 Research Plan

In order to achieve our research objective for synthesis of nano-Hap, following studies were done:

- The thermal properties of the as-synthesized HAp powder were studied using Thermogravimetric (TG/DTA)
- Phase characterization of HAp powder using Fourier Transform Infrared Spectroscopy (FTIR)
- Phase characterization and calculation of average grain size of the as-synthesized and calcined powder by X-ray diffraction (XRD)
- Morphology and particle-size study of the as-synthesized HAp powder by High-resolution Transmission Electron Microscopy (HR-TEM)

- Densification study of the sintered specimens
- Study of phase evolution as a function of sintering temperature by XRD
- Microstructure evolution as a function of sintering temperature by Scanning Electron Microscopy (SEM)
- Characterization of mechanical properties of the sintered specimens though biaxial flexural strength and Vickers hardness tests
- Study of biodegradation and biomechanical properties of sintered HAp samples was done in Simulated Body Fluid, maintained in a dynamic state, as a function of time.

Figure 2 is a schematic of the research plan adopted and followed in this study.

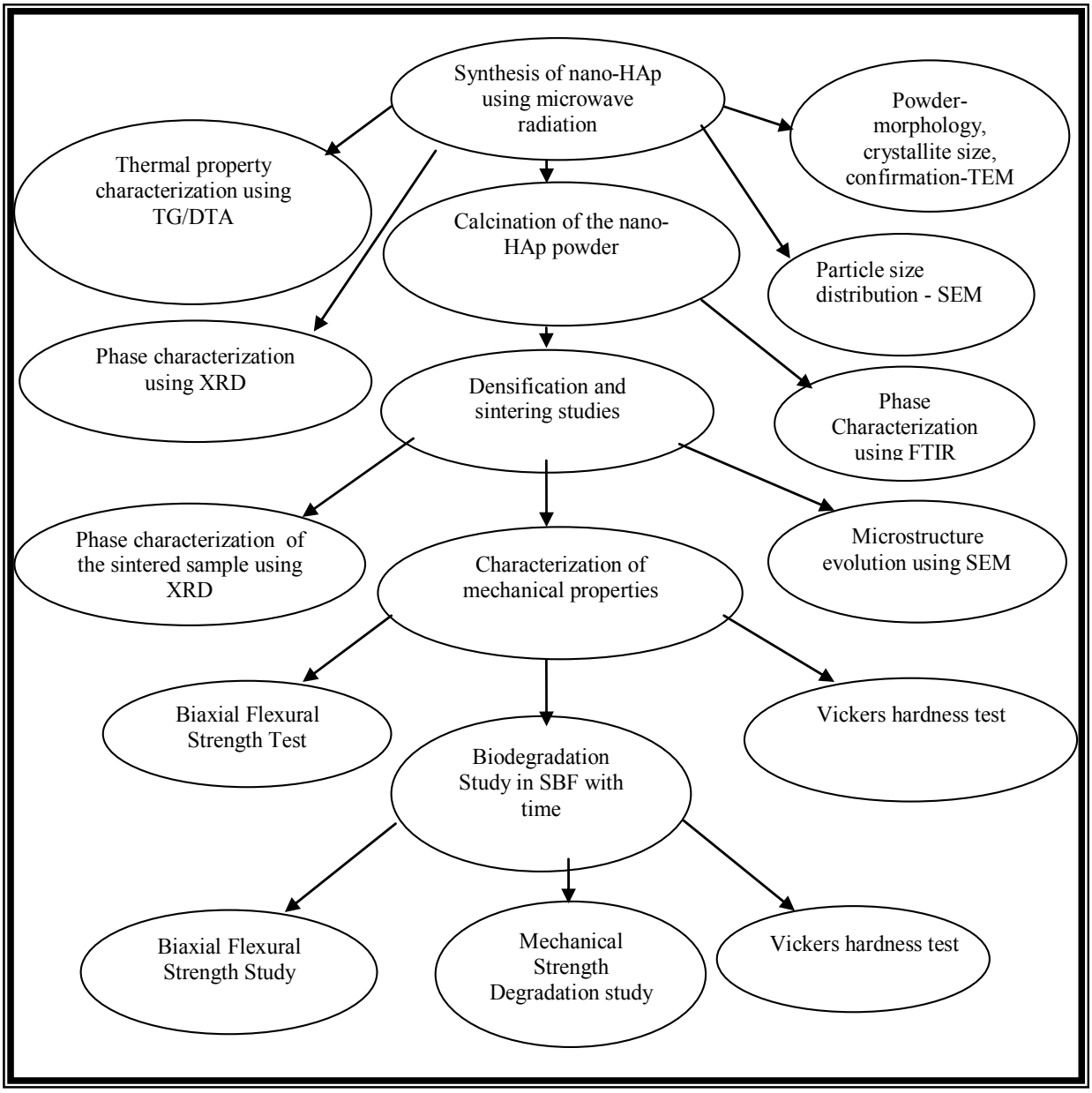

Figure **2**: Schematic of Research plan for nano-HAp Synthesis and Characterization

Mechanical properties of nanocrystalline TiO_2 powder were also studied in this research. Synthesis of nano-TiO_2 powder was accomplished previously using a simple sol-gel process established by Mr. Qiu Shipeng in our laboratory.

To study the mechanical properties of nanocrystalline TiO_2, following studies were done:

- Densification study of the sintered specimens.
- Characterization of mechanical properties of the sintered specimens though biaxial flexural strength and Vickers hardness tests.
- Study of biodegradation and biomechanical properties of sintered TiO_2 samples was done in Simulated Body Fluid, maintained in a dynamic state, as a function of time.

Figure 3 is a schematic of the research plan adopted and followed in this study.

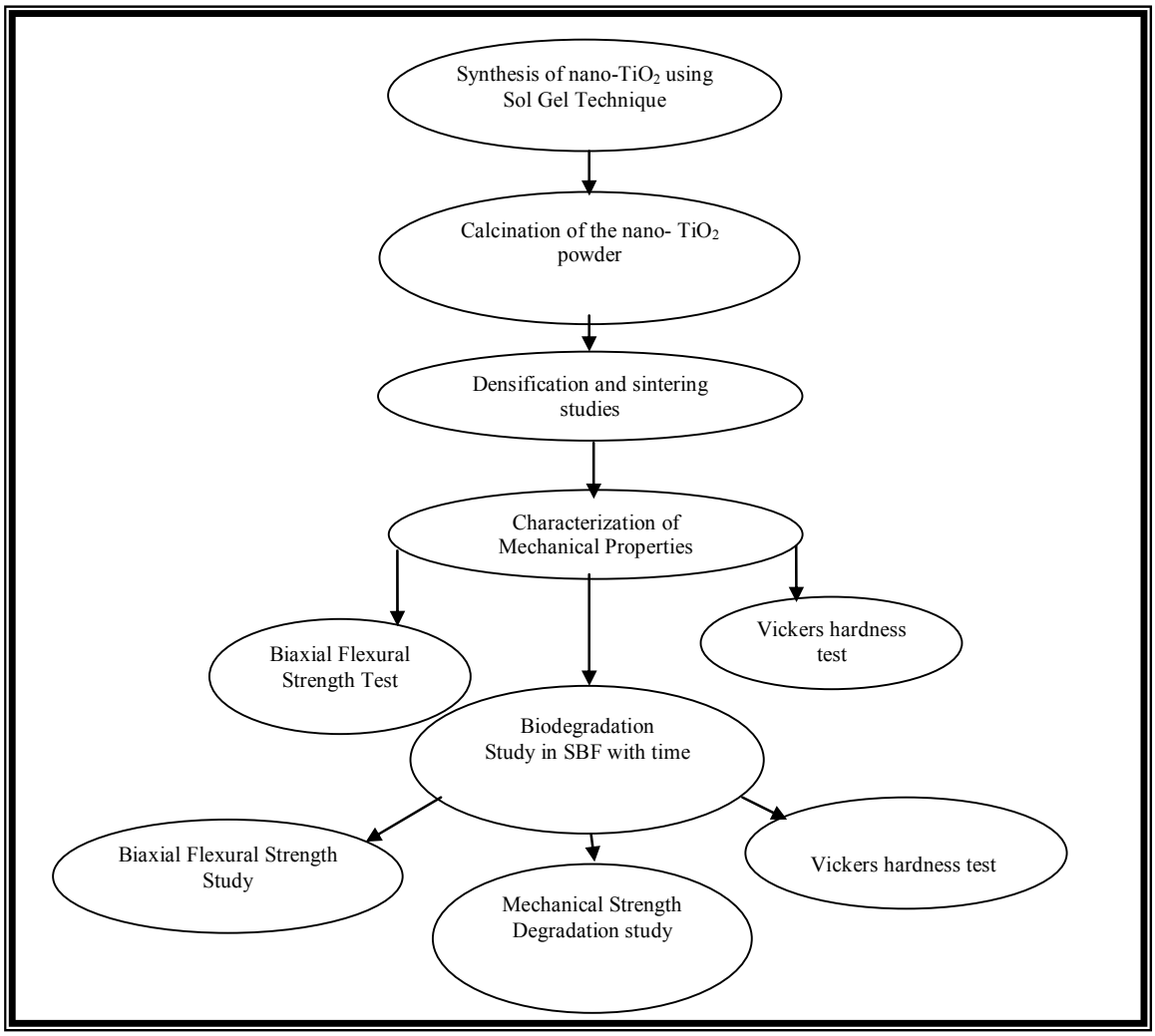

Figure 3: Schematic of research plan for nano-TiO_2 synthesis and characterization

2. LITERATURE REVIEW

2.1 Nanocrystalline Bioceramics

Novel ceramics which can be used to replace bone defect without any toxic response inside the body are called bioceramics. Nanotechnology has revolutionized the field of material science as complex structures for bone tissue engineering can be easily achieved. Nanocrystalline bioceramics are preferred in clinical uses because of their advantages such as low density compared to metals, high compressive strength and high hardness, good corrosion and wear resistance, aesthetically pleasing (for dental applications), and compositional similarity with bone resulting in improved biocompatibility. These bioceramics can be classified as Bioinert, Bioactive, and Bioresorbable. Bioinert ceramics don't interact with the surrounding tissue unlike bioactive ceramics which interact with the surrounding tissue and bond with them whereas bioresorbable ceramics degrade with time and get replaced by surrounding tissue.

Bioceramic can be used for structural applications like joint or tissue replacement or as a coating for metallic implants to improve their biocompatibility. Calcium Phosphate Ceramics (HAp, Tricalcium Phosphate and Tetra Calcium Phosphate), Alumina, Zirconia, Bioglass or Bioactive glasses and Pyrolytic Carbon have been used for bone repair [6, 7]. These ceramics can be inert, bioactive or bioresorbable. These ceramics can also be used for orthopedic, dental and maxillofacial, prosthetics, Alveolar ridge augmentation, load bearing applications etc.

Properties of these ceramics can be greatly modified by reducing the particle size to nano- scale as surface to volume ratio increases [5] which provides more substrate surface for cell adhesion and proliferation. High volume fraction of grain boundaries in nano-scale ceramic

compacts increases ductility and plasticity [8]. In 1987, Karch *et al*. reported that with nano-grain size, brittle ceramics exhibit large amount of plastic strain [9]. Nano-biomaterial promotes osteoblast adhesion and proliferation, osteointegration and deposition of calcium containing minerals on its surface [10]. So, mechanical and biological properties can be greatly tailored by changing powder morphology. Only problem with the bioceramics is its poor mechanical strength. Nano-technology can be of great help in improving mechanical properties and bioactivity or resorbability.

Angstrom Medica developed Nanoss bone filler from nano-crystalline Calcium Phosphate. Because of its excellent bioconductivity, it can be used to replace human bones. It is believed to be the first nano-crystalline material to get clearance from US Food and Drug Administration in 2005. Calcium phosphate is precipitated in aqueous medium and then the obtained precipitate is compressed and heated to form Nanoss [11].

Zinc Phosphate nano-ceramics can be used for oral insulin Delivery with pH sensitive coating to prevent insulin particles from Hydrolysis and enzymatic degradation. Dry Zinc Phosphate nano-particles were soaked in insulin and then coated with Sodium alginate. Release profile of insulin in vitro was promising toward development of non-invasive oral drug delivery system for diabetic [12].

Among all the available bioceramics, calcium phosphates are materials of choice for bone tissue repair because of their similarity of composition with bone mineral; excellent bioactivity; ability to promote cellular expressions; and osteoconductivity. Particularly, the bioactive hydroxyapatite phase shows excellent biocompatibility and osteoconductivity and elicits specific

biological responses at the interface of the material, which results in the formation of a strong bond between the bone tissues and the material.

2.2 Nano-crystalline Hydroxyapatite

HAp is a material of choice for various biomedical applications like orthopedic, dentistry, drug delivery, because of its similarity of composition with mineral phase of the bone, excellent biocompatibility, and ability to promote cellular functions and expression and osteoconductivity. They elicit specific biological responses at the interface of the materials which results in the formation of strong bond between bone tissue and material. Coating of HAp is applied to metallic implants to enhance their surface properties.

Hydroxyapatite, $Ca_{10}(PO_4)_6(OH)_2$, possesses a hexagonal structure with a P63/m space group and cell dimensions a=b=9.42Å, and c=6.88Å, where P63/m refers to a space group with a six-fold symmetry axis with a threefold helix and a mirror plane [13, 14]. Crystal structure and lattice parameter of HAp are well represented in Figure 4 [15, 16].

Non-Stoichiometry of HAp is due to substitution of Ca^{2+}, PO_4^{3-} and/or OH^- ions by atoms or groups such as halogen atoms or carbonate ions. Though it shows excellent biocompatibility, its mechanical strength under complex stress-states is poor. It has been found useful for non-load-bearing applications such as bone fillers, building material to create porous scaffolds to promote bone formation, and as coatings on metal prostheses to improve bioactivity.

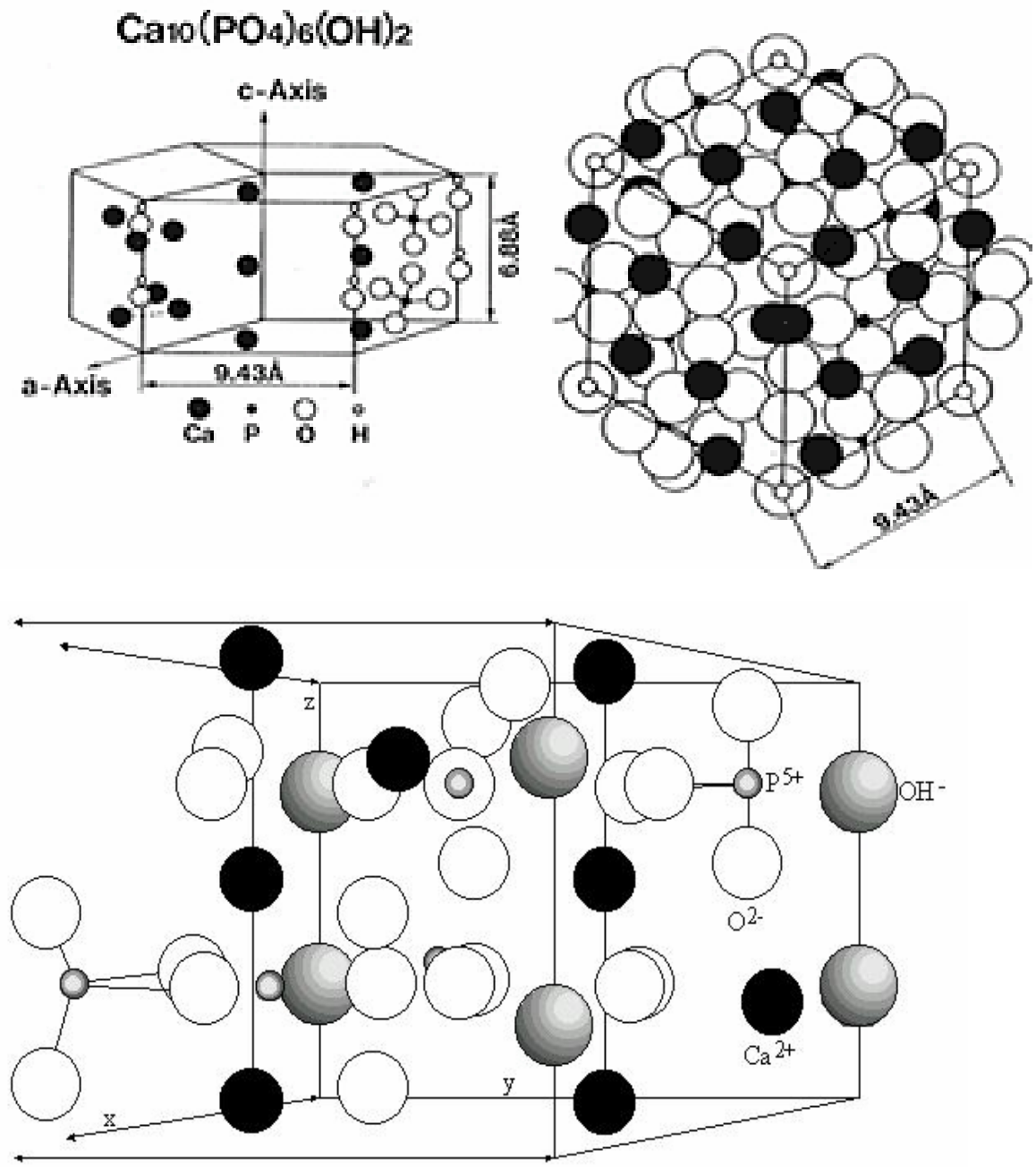

Figure 4:Crystal structure of Hydroxyapatite synthesized in Simulated Body Fluid in SBF at 37^{o}C [15, 16]

However, there is a significant difference of properties between natural apatite crystals found in the bone mineral and the conventional synthetic HAp. Bone crystals are formed in a biological environment though the process of biomineralization and are nano-sized. The resorption of bone mineral by osteoclasts is quite homogeneous. Synthetic HAp on the contrary, presents a low surface area and has strong bonding which result in a two stage resorption process: disintegration of particles and dissolution of the crystals [17].

HAp powder can be produced by wet methods [18], solid state reaction [19], Sol gel [20], electro-crystallization [21], Spray pyrolysis [22], Emulsion processing [23], Mechanical and hydrothermal treatments [24],Chemical precipitation and hydrothermal technique are capable of producing n-Hap [25, 26]. Precipitation of Calcium phosphate is very much dependent on Stoichiometry, pH, rate of addition, ionic strength, temperature etc [27] so these parameters should be precisely controlled.

Novel method to synthesize ceramic on nano-scale is microwave synthesis. Microwave is an electromagnetic wave of high frequency which consists of alternate magnetic field and electric field. Microwave excitation heats the core and surface of the material homogeneously because of microwave energy transfer to thermal energy by collision between rotating molecules. Microwave energy is responsible for the intensive movement of the substance molecules in the solution. Microwave energy of high frequency gets absorbed by bound water in the sphere of hydration of a polyvalent ion. Absorption of microwave energy weakens the bond between calcium ions and its sphere of hydration facilitating deaquation which is a must for apatite formation in aqueous solution [28].

HAp is the most stable form of Calcium Phosphate at normal temperature and in the pH range 4-12 with Ca/P ratio being 1.67 [29]. Nano-Hap powder was prepared using precipitation reaction using Calcium hydroxide and Diammonium hydrogen phosphate. Immediately after mixing the chemicals they are subjected to microwave radiation and white precipitate is obtained. Due to irradiation ammonia was eliminated. Majority of nano-HAp particles prepared were 50 nm in diameter and 200 nm in length. As-prepared precipitate was calcium deficient HAp with PO_4^{3-} ions substituted by CO_3^{2-} ions.

Parhi *et al* [30] prepared HAp though a novel microwave-mediated metathesis reaction. Solid Mixture of Calcium Chloride ($CaCl_2$) and Sodium Phosphate (Na_3PO_4) was irradiated in microwave oven. Irradiated powder was washed and dried to obtain n-HAp. Sodium Chloride (NaCl) acted as a heat sink in this metathesis reaction of HAp synthesis.

Han *et al.* [31] synthesized nano-HAp by microwave-hydrothermal method using Phosphoric acid (H_3PO_4) and Calcium hydroxide ($Ca_9(OH)_2$) in a closed vessel microwave device. Applied microwave power and Ca/P ratio played an important role in determining the purity of HAp. At 550 W power and Ca/P ratio of 1.67, nano phase of HAp was observed with two morphologies. Level of the impurity in the synthesized powder was below 50ppm.

Yang *et al.* performed some experiments to study the effect of aging time & irradiation time and power of microwave on thermal stability of HAp [32]. HAp was prepared using Ammonium Hydroxide, glucose and Calcium nitrate tetra hydrate. It was observed that thermal stability of HAp is strongly dependent on aging time, microwave irradiation time and power and increases as all the above parameters increases. In short irradiation and aging time, calcium deficient HAp [$Ca_{10-X}(PO_4)_{6-X}(OH)_{2-X}$] was formed which affects the thermal stability.

S.Jalota *et al*. [33] discussed the synthesis and characterization of a new Rhenanite (β $NaCaPO_4$) and HAp biphasic biomaterial for skeletal repair. Rhenanite is derived from Rhenania Process. This process is used in fertilizer industry to get soluble phosphate material. In this process, natural HAp mineral is mixed with Na_2CO_3 and SiO_2 where SiO_2 is added to prevent the occurrence of free CaO in sintered powder. Powder mixture is grinded and calcined in rotary kiln for few hours in the temperature range of 1000-1200^oC. Resorbable bone graft materials based on $NaCaPO_4$ are already available in the market. In-vivo $NaCaPO_4$ is supposed to supply Ca^{2+} ions as well as hydrogenated phosphate ions to the surrounding tissue on implantation. $NaCaPO_4$ is expected to be osteoinductive stimulant in the body. β-$NaCaPO_4$ has an orthorhombic (space group Pnam [34]) unit cell with lattice parameter of a=6.797, b=9.165 and c= 5.406 Å [35].

Kilian *et al*. [36] showed that sintered HAp implant stay at the site for years after surgery where as β TCP has significantly higher solubility as compared to HAp and gets resorbed easily even before the completion of new bone [37, 38]. Attempts have been made in this direction to develop a new composite with high in vivo resorbability and osteoinductive/osteoconductive capability. Recently, it has been proved that β Rhenanite (β $NaCaPO_4$) is an alkali calcium phosphate which supports cellular proliferation together with expression of osteogenic marker much higher than β TCP [39]. Ramselaar and coworkers studied the biodegradation rate of $NaCaPO_4$ in comparison to HA and β TCP in vivo [40-43]. They demonstrated that rate of bone deposition on the surface of β $NaCaPO_4$ is much more than HAp and it has strong prospective in developing bioresorbable or osteoinductive calcium phosphate bioceramics. Knabe *et al*. [44] noticed high solubility of $NaCaPO_4$ samples in vitro rat bone marrow cell test. Kangasniemi *et al*.

[45] proved that the compound containing β $NaCaPO_4$ has positive effect on the rate of growth of apatite layer on the surface of samples soaked in Simulated Body Fluid (SBF).

Y.Doi e al [46] developed a new Calcium Phosphate Cement with sodium calcium phosphate ($Na_3Ca_6(PO_4)_5$). It was observed that cement powder containing $Na_3Ca_6(PO_4)_5$ in addition to tetracalcium phosphate and β TCP and tetracalcium phosphate sets in 3-7 minutes when mixed with 30wt % malic acid or citric acid at a powder liquid ratio of 3:1 with compressive strength around 52 or 27 MPa. It was also noticed that cement with sodium calcium phosphate ($Na_3Ca_6(PO_4)_5$) when mixed with malic acid or citric acid was far less toxic than the commercial carboxylate cement used as negative control in He-La cell culture. Culture experiments conducted with osteoclast proved that number of osteoclasts was far much greater on cement with sodium calcium phosphate mixed with malic or citric acid as compared to commercial carboxylate cement.

Nikahira *et al.* [47] did SBF study on HAp samples and HAp samples containing $NaCaPO_4$ by placing the samples in SBF for 4-7 days. No deposit of bone like CaP was observed on the surface on HAp where as HAp samples containing $NaCaPO_4$ were covered with such deposit. High dissolution rate of HAp samples containing $NaCaPO_4$ is due to the presence of Na+ ions which weakens the bond between Ca^{2+} and PO_4^{3-}

According to Gong *et al* [48] β-$NaCaPO_4$ act as a nucleation precursor for the formation of calcium phosphate.

$$NaCaPO_4 + 2\ Ca^{2+}\ H_2O \rightarrow Ca_5(PO_4)_3OH + 3Na^+ + H^+ \qquad \text{equation(1)}$$

Sodium calcium phosphate [$Na_3Ca_6(PO_4)_5$] and amorphous silicon phases were developed by sintering HAp and Bioglass ® (BG) at 1200°C [49]. It was observed that thick layer of apatite covered the surface of sodium calcium phosphate samples after one week immersion in SBF solution maintained at 37^oC and ph of 7.4

Poor mechanical properties limited the use of nano-HAp in the field of biomedical applications. Various investigations have proven that the mechanical strength and sintering temperature of HAp are strongly dependent and mechanical strength of dense HAp decreases sharply with the decomposition of HAp [50, 51]. Mechanical & biological performance of HAp can be tailored by changing powder characteristics such as particle size, shape, their distribution, and agglomeration [52]. Nano-HAp provides large surface area which makes it very active for cell proliferation, synthesis, of alkaline phosphate and deposition of calcium containing minerals [53]. Brittle nature and low fracture (<1MPa $m^{1/2}$) toughness of HAp limited its use in load-bearing applications [54, 55]. Mechanical strength and fracture toughness of HAp can be improved by addition of low melting secondary phase for better densification [56-58], addition of sintering additives to increase densification by grain boundary strengthening [59-61] and use of nano scale powder to improve densification due to larger surface area to volume ratio.

Nano-HAp and polyamide composite is almost similar to bone so its bio-performance in osseous environment is good [62]. Polyamide is responsible for imparting toughness and mechanical strength to this composite whereas nano-HA accounts for excellent bioactivity. This composite was prepared using nano-HAp slurry and co-solution method under normal atmospheric pressure. Nano-HAp powder maintains its original morphology with crystal size 10-

30 nm in diameter by 50-90 nm in length. HAp was uniformly distributed in the polyamide matrix.

HAp-reinforced UHMWPE (Ultra High Molecular Weight Polyethylene) was developed to from synthetic biocomposite to match with the properties of natural bone [63]. Powder HA (Volume fraction=0.5) and UHMWPE were mixed and compounded by twin extrusion using oil as swelling agent. Using hot press and extraction, oil was removed. The yield strength of the composite was comparable to the cortical bone [64].

Liao *et al.* (2005) [65] developed nano-HA/collagen/PLGA composite for bone tissue engineering. It can be used for repairing periodontal defects, membranes for covering bone defects, skin wound repair and healing, skin sealing and a carrier for antibiotic, bone growth factors because of its flexibility, strong mechanical strength, easy manipulation character, excellent biocompatibility and controlled resorption.

Fu *et al.* [66] reported that when n-HAp was introduced in GBC, it slows down the growth rate of cancer cells U2-OS (Osteosarcoma) and increases the mechanical strength of the composite. It is a great material for bone repair after tumorotomy operation.

HA has been reported to show cell-inducing effect on the formation of cornea tissue [67]. PHEMA (Poly2hydroxyethylmethacrylate) has widely been used as cornea material for cornea implant. Bio-inert nature of PHEMA creates trouble with the combination between the material and peripheral cornea tissue resulting in bad implant. Nano-HA layer was developed on the PHEMA by sol dipping method to improve the cyto-affinity of the polymeric material [68]. HAp particle coating and aggregation improves the adhesion mechanism of cornea fibroblast to the membrane.

Bacterial infection has always been serious problem due to various percutaneous devices such as blood tubes, catheters etc. HAp is being tested in making percutaneous device to prevent infection. Furuzono *et al*. (2004) showed fabrication and adhesion properties of a scaffold made of nano-scaled HAp/Polymer complex with silk fibron (SF) substrate to develop a percutaneous device [69]. HAp proved to be good adhesive surface for cells. This research is relatively new. Animal experiments are being conducted with percutaneous implantation to test infection-protection properties and cell adhesion.

Suspension of Calcium phosphate and DNA has been used for many decades to carry out transfection in cells. Zhu *et al.* [70] identified that nano-HAp particles can transfect certain plasmid DNA into cell of interest. The experiment was performed using gastric cancer SGC-7901 cells. Nano-HAp particles have no adverse effect in-vivo and compatible with the invitro cell culture. Nano-HAp was prepared by mixing Calcium nitrate ($Ca(NO_3)_2$) and Ammonium Phosphate ($(NH4)_2HPO_4$) while maintaining Ca/P ratio of 1.67. Ammonia was added to adjust pH.

Nanostructure of HAp helped in improving its sinterability, ductility, superconductivity and mechanical strength of the ceramic. With the use of nanotechnology, formulating various polymers, ceramics and polymer- ceramic composites to engineer bio compatible, active and degradable materials holds lot of promise for fields like tissue engineering.

2.3 Nano-crystalline Titanium dioxide

TiO_2 exists mainly as anatase, rutile and brookite. Anatase have tetragonal structure with space group D_{4h}^{19} -$I4_1/amd$ space group and lattice constant a=0.3733 nm, c=0.937 nm, c/a=2.51 where as Rutile have tetragonal structure too, but belongs to space group D_{4h}^{14} -$P4_2/m$ nm and lattice constant a=0.4584 nm, c=0.2953 nm, c/a=0.664 [71]. Rutile and Anatase are widely used because of their unique properties. Brookite have rhombohedral structure with lattice constant a=0.5436 nm, b=0.9166, c=0.5135,c/a=0.944. They are used in solar cells as photocatalyst, in ceramics as optical coating, to provide corrosion resistance to the metallic implants etc. Roy *et al.* studied the effect of TiO_2 nano-tube on the blood clotting kinetics [72]. Blood in contact with dispersed TiO_2 nano-tube and blood in touch with gauze pad surface-decorated with TiO_2 nano-tube improved blood clotting strength and significantly reduced clotting time. In comparison TiO_2 nano-particles form cots of weak strength and increased clotting time. It was noticed that clotting time reduced by 10% when blood was in contact with gauze pad decorated with TiO_2 nano-tube or dispersed TiO_2 nano-tube. Strength was found to increase by 75% in the above cases whereas Anatase TiO_2 nano-particle decreased the clot strength of the original blood by 9% and increased clotting time too.

TiO_2 can also be used for disinfecting surfaces by the mechanism of photo catalytic oxidation using UVA light [73]. Depth of penetration is not adequate when only hard UVC light is used for disinfection. Highly reactive OH^- radicals are produced on the surface coated with TiO_2 in the presence of water and oxygen due to photocatalytic oxidation caused by mild UVA. OH^- radicals reduce the bacterial contamination by killing bacteria.

TiO_2 can also be used for photo-assisted degradation of organic molecules. TiO_2 being a semiconductor produces electron hole pairs when irradiated with sunlight. Charge carriers react with adsorbed water and oxygen on the surface to form free radicals. These radicals lead to complete decomposition of organic molecule into carbon dioxide and water [74].

Martin *et al.* [75] discussed the use of TiO_2 (Semiconducting Metal oxide) in photolytic artificial lung. Artificial lungs deliver oxygen to the blood using hollow tubes or fibers. To eliminate the use of tubes, pyrolytic energy was used to produce oxygen from the water present in blood. Indium oxide, anatase TiO_2 and MnO_2 were deposited on fused silica by magnetic sputtering. TiO_2 layer was laser radiated to produce electron-hole pairs to catalyze redox reaction with water in the blood. TiO_2 should have significant porosity and surface area to allow proper reaction between produced holes and water in the blood. Free electrons are conducted away. MnO_2 was also used as catalyst to dissolve oxygen in the blood. This process increased the blood oxygenation as much as 90%.

3. METHODOLOGY

In this chapter, the whole experiment is discussed in details, starting from raw material selection, synthesis and characterization of as-synthesized nano-HAp powder.

3.1 Materials

Table 3: Chemicals used for nano-Hydroxyapatite synthesis

Chemical Name	Molecular Formula	Purity	Company
Sodium phosphate dibasic anhydrous	HNa_2O_4P	≥99.5%	Fluka Biochemika
Calcium nitrate tetrahydrate	$Ca(NO_3)_2.4H_2O$	99%	Alfa Aesar
Ethylenediaminetetraacetic acid	$C_{10}H_{14}O_8N_2Na_2.2H_2O$	0.1M	Fluka
Ammonium hydroxide	NH_4OH	5N	Ricca Chemical

Table 4: Chemicals used for nano-Titanium dioxide synthesis

Chemical Name	Molecular Formula	Purity	Company
Titanium (IV) tetraisopropoxide	$Ti[OCH(CH_3)_2]_4$	98+%	Fisher Scientific, USA
Isopropanol	$CH_3CH(OH)CH_3$	70%	Fisher Scientific, USA
Nitric acid	HNO_3	6M	Fisher Scientific, USA
Titanium dioxide (0.43µm)	TiO_2	99.9%	Alfa Aesar, USA

3.2 Microwave Synthesis of Nanocrystalline Hydroxyapatite Powder

All reagents used in this study were analytical grade and used without further purification. In a typical procedure, 5 ml of a mixed solution of calcium nitrate tetrahydrate [$Ca(NO_3)_2 \cdot 4H_2O$ (0.1M, Alfa Aesar Ward Hill, MA)] and EDTA (0.1 M, Fluka Biochemica, Germany) was added to 25 ml solution of sodium phosphate dibasic anhydrous (Na_2HPO_4, Fluka Biochemica, Germany). While mixing Ca/P ratio was maintained at 1.67. The pH of the final solution was adjusted to 9 by adding ammonium hydroxide (NH_4OH with pH10, ACROS organics Fairlawn, NJ) solution. After stirring for several hours, the aqueous solution with a pH 9 was microwaved in domestic microwave of 600 W power (Sunbeam, 5 Power level) as shown n Figure 5 locally customized with a refluxing system. The working cycle of microwave was 3 min in ON position followed by a 5 min OFF position for a period of 20 min.

The final solution was allowed to cool to room temperature inside the microwave and then the precipitates were filtered using filer paper. The obtained precipitates were dried in a manual muffle furnace in air at 200^oC for 4 h. The product was ground into fine powder using a mortar and pestle. The resultant powder was then characterized using various techniques for properties. Additionally, some powder was calcined at 500^oC for 2 h in a muffle furnace to study the effects of calcination on phase evolution and crystallite size. Ammonia by-product was eliminated from the mixture due to irradiating heat.

Figure 5: Set up showing microwave sythesis of HAp nanopowder

The synthesis parameters were optimized by modifying mixing time (t_1) for calcium nitrate tetrahydrate and EDTA with sodium phosphate dibasic anhydrous solution, stirring time (t_2) after adding NH4OH, pH of final solution and microwaving time (t_2). Table5 shows the parameters varied during the entire experiment for the synthesis of nano-HAp power.

Table 5: Synthesis parameters for HAp powder synthesis

Experiment No.	**Mixing time** (t_1,min)	**Stirring time** (t_2, min)	**pH of final solution**	**Microwaving time** (t_2, min)	**Output**
1	60	5	9	20	Small amount of powder
2	240	5	9	20	Enough amount of powder
3	1440	5	9	20	Same amount as in Exp-2
4	240	30	9	20	No powder
5	240	10	9	20	No powder
6	240	15	9	20	No powder
7	240	5	< 9	20	No powder
8	240	5	9	5	Amorphous powder
9	240	5	9	10	Small amount of powder
10	240	5	9	20	Enough amount of powder

3.3 Sol-Gel Synthesis of TiO_2 Nano-powder

Synthesis of nano-TiO_2 powder was accomplished previously using a simple sol-gel process established by Mr. Qiu Shipeng in our laboratory. Titanium tetraisopropoxide (TTIP), isopropanol and deionized water were used as precursor material for the synthesis of TiO_2 nano-powder. TTIP solution was titrated with homogeneous solution of water and isopropanol while

stirring. After titration Nitric acid was added to the final solution and pH of the solution was maintained at 2. The solution was stirred for 1h and then peptized for 24 h. After peptization two layers of solution were formed. Upper layer consisting of organic byproduct of hydrolysis was removed from the bottom layer consisting of Titania acid gel. This gel was dried at 110^{o}C in a muffle furnace until yellow color crystals appeared. These crystals were crushed into fine powder using mortar and pestle and calcined at 400^{o}C for 3 h.

3.4 Characterization of the synthesized HAp nano-powder

3.4.1 Thermogravimetric Analysis (TGA) and Differential Scanning Calorimetric (DSC)

Thermal analysis of the synthesized nanocrystalline HAp powder was performed in a PYRIS Diamond Differential Thermal Analyzer (DTA) by Perkin-Elmer Instruments, Waltham, MA. The Diamond DTA is unique in offering higher sensitivity and provides insights information on materials. The design allows sophisticated analysis when performing the direct measurement of heat flow into or out of a sample as the sample and reference pans are heated by two independent furnaces embedded in a temperature-controlled heat sink. TGA determines a material's thermal stability and measures the weight loss or gain of a material as a function of temperature. Mostly, TGA analysis is performed in an atmosphere i.e. air or oxygen with a linear ramp of temperature. The maximum temperature should be so selected that the weight of the specimen is stable at the end of the experiment. This basically indicates that all chemical reaction are complete i.e. the whole of carbon is burnt and only metal oxides are left over. DSC

measurements indicate endo or exothermic reaction or possible phase transition. The experiment was performed in helium gas inert atmosphere. Sample weight was 0.65 mg. Helium gas flow speed of 160cm^3/min was employed. Thermogravimetric (TG) analyzer was used to find the weight loss during heating between 45^oC and 1200^oC at the rate of 20^oC/min in helium atmosphere. Sample was initially heated to 130^oC for conditioning and to remove some physically absorbed moisture and organic impurities. After conditioning, the specimen was cooled to 45^oC and heated again to 1200^oC at a heating rate of 20^oC/min.

3.4.2 Fourier Transform Infrared Spectroscopy (FTIR)

FTIR is a powerful tool for identifying types of chemical bonds in a molecule by producing an infrared absorption spectrum. Fourier transform spectrograph is much more sensitive and has a shorter sampling time than other conventional spectroscopic techniques. Data is collected and converted from an interference pattern to a spectrum. The wavelength of light absorbed is characteristic of the chemical bond and thus by interpretation of the infrared absorption spectrum the chemical bond in a molecule can be determined. Depending on the element and the type of bonds, molecular bonds vibrate at various frequencies. Fourier transform infrared (FT-IR) spectroscopy was performed on finely ground HAp nano-powder calcined at different temperature using a Perkin Elmer spectrum 100 spectrometer to distinguish the types of calcium phosphate formed. The spectral range used was from 650 cm^{-1} to 4000 cm^{-1}. Heat treated specimens were finely powdered using a mortar and pestle prior to obtaining the measurement. The baseline of the entire spectrum was corrected for the accuracy of results.

3.4.3 X-ray Diffraction (XRD)

XRD analysis was performed on an as-synthesized and calcined powder and on compacted sintered structure to study the phase evolution, crystallite size and crystal structure. XRD patterns were recorded in the 2 θ range of 20-45° with the help of automated X-ray diffractometer (Model D/MAX-B, Rigaku Co., Tokyo, Japan) using Cu Kα radiation (λ=1.5418 Å) at 40 KV and 30 mA setting. Scanning rate of 1°/minute and 2 θ step size of 0.05° were used. Observed XRD pattern was compared with the standard pattern available from PDF card for phase characterization.

The crystallite size of the synthesized powder was determined from the XRD patterns using the Scherrer's equation (1):

$$\beta = [0.9\,\lambda / (\langle d\rangle \cos\theta)] \qquad \text{equation (2)}$$

Where λ is the wavelength of X-ray, θ is the Bragg angle, ⟨d⟩ is the average crystallite size, and β is the full width at half maximum.

Peak broadening is observed in the X-ray diffraction pattern which may be due to the Instrumental effect, Crystallite size and lattice strain [76]. Instrumental effect may include peak broadening due to imperfect focusing or unresolved α1 and α2 peaks. Peak broadening also occurs with the decrease in particle size. Broadening caused by strain in the material can be represented by:

$$B_{strain} = \eta \tan\theta \qquad \text{equation(3)}$$

Where η represents strain in material

To calculate the accurate grain size, peak broadening due to lattice strain, strain due to crystallite size and instrumental effect should be subtracted from B (Peak width at half maximum intensity). After deducting peak broadening due to instrument remaining peak broadening can be represented by:

$$B_r = k\lambda / L\cos\theta+\eta\tan\theta \qquad \text{equation (4)}$$

Where K is a constant generally taken as 0.9, λ corresponds to wavelength, L is average particle size and θ is the Bragg's angle.

By plotting $B_r\cos\theta$ against $\sin\theta$, straight line with slope η is obtained which intersect Y axis making intercept of $k\lambda/L$ from which L can be calculated.

3.4.4 Scanning Electron Microscopy (SEM)

Scanning and transmission electron microscopy techniques were used to study and analyze morphology, agglomeration and size of hydroxyapatite particles in the synthesized powder. SEM technique was employed to observe the particle-size and agglomeration of the as-synthesized nano-HAp powder. For this, a very small amount of powder was placed on an adhesive carbon tape, coated with gold/palladium in Magnetron Sputter Coater from Emitech Inc. for 1minute and then observed in a JOEL SEM (Model 6400F, JEOL, Tokyo, Japan). Particle size of the synthesized powder was further investigated using IQ Materials Image Analysis software from SEM micrographs. The particle size module of IQ materials Image Analysis software automatically detects and measures particles pictured in captured images. This software makes its initial measurements in terms of pixels. The calibration was done to

convert these to more meaningful units, such as millimeters, micrometers etc for the image under analysis. Specific area of interest in the image can be analyzed using this software. The more image data you analyze, the more accurate your results will be. This module provides valuable information regarding measurable characteristics of particles, including size measurements, location information and easy thresholding tools for identifying particles of interest in images, shape and orientation measurements (for example, degree of circularity and angle of rotation) and ability to control particle recognition by setting a minimum size requirement.

3.4.5 Transmission Electron Microscopy (TEM)

The morphology, grain size and the lattice fringes of the as-synthesized HAp nano-powder were characterized using H-TEM, Model Tecnai - Philips F30, FEI Co., Hillsboro, OR). It can capture images with a maximum magnification of 10,000,000X and resolution of 0.02 nm point to point. This machine operates with a field emission gun and can operate at a maximum voltage of 300 KV. Presence of well defined dots and ring patterns conform the presence of crystalline phase in Selective Area Diffraction Pattern (SAED). To perform TEM analysis, formvar-carbon coated grid was dipped into the synthesized powder. The grid was observed under a Tecnai H-TEM for analysis. Energy dispersive X-ray spectroscopy (EDS) was performed for chemical microanalysis using an EDAX system attached to H-TEM. Selective area diffraction pattern (SAED) was also obtained to confirm crystallinity of the synthesized powder.

3.5 Powder Compaction

As-synthesized powder was calcined at 200°C for 4 h to remove the carbonaceous impurities. This calcined powder was used as a starting material for compaction and sintering studies. Using Cold Compaction, powder was pressed into pellets and sintered for further research.

3.5.1 Cold Uniaxial Compaction

Nano-powder used for compaction was grinded after calcination to break any possible agglomeration. Traditionally Cold die compaction method was used to achieve dense structures by powder rearrangement including sliding and rolling. For compaction of nano-HAp and nano-TiO_2 into dense cylindrical specimen or green samples cylindrical mould was used at a pressure of 78.69 MPa in a uniaxial single action manual hydraulic press (Model 3851-0, CARVER INC., Wabash, IN). To reduce the friction between powder and the mould, a dry film of PTFE (Dupont Krytox) was sprayed on the inside surface of mould and punch. Nano-HAp and nano-TiO_2 samples prepared for studying densification, hardness and biaxial strength were having an average diameter of 9.5 mm and 1.8 mm in thickness.

3.5.2 Sintering and Densification

All the compacted samples or green samples were sintered in a programmable high temperature muffle furnace (Model 46100, Barnstead International Co., Dubuque, IA) in open air. Nano-HAp samples were sintered in the temperature range of 1100-1250^{o}C for 4.5 h whereas

nano-TiO_2 samples were sintered at 1400^oC and 1500^oC. Six samples were sintered at every temperature to study the sintering and densification behavior. To improve densification and avoid cracks due to stresses in the sintered samples, suitable sintering cycle with several soaking temperatures was adopted.

3.6 Characterization of Sintered HAp structures

3.6.1 Fourier Transform Infrared Spectroscopy

FTIR is a powerful tool for identifying types of chemical bonds in a molecule by producing an infrared absorption spectrum. Fourier transform spectrograph is much more sensitive and has a shorter sampling time than other conventional spectroscopic techniques. Data is collected and converted from an interference pattern to a spectrum. The wavelength of light absorbed is characteristic of the chemical bond and thus by interpretation of the infrared absorption spectrum the chemical bond in a molecule can be determined. Depending on the element and the type of bonds, molecular bonds vibrate at various frequencies.

3.6.2 Phase Analysis using X-ray Diffraction Technique

To study the phase change with the increase in sintering temperature of nano-HAp, X-Ray Diffraction pattern were recorded at different temperatures using (Model D/MAX-B, Rigaku Co., Tokyo, Japan) and compared with the standard ones.

3.6.3 Densification Study

All of the six pressed samples were sintered at different temperature in a programmable high temperature muffle furnace (Model 46100, Barnstead International Co., Dubuque, IA) in open air and observed sintered density was compared Nano-HAp samples were sintered in the temperature range of 1100-1250^{o}C for 4.5 h whereas nano-TiO_2 samples were sintered at 1400^{o}C and 1500^{o}C.

3.6.4 Microstructural Analysis

To study the grain growth or grain coarsening of sintered nano-HAp samples with the increase in temperature Scanning Electron Microscopy was used. Samples for SEM study were gold coated in Magnetron Sputter Coater from Emitech Inc. for 1minute. After coating, samples were analysed in JOEL SEM (Model 6400F, JEOL, Tokyo, Japan).

3.6.5 Mechanical Characterization

Vickers Hardness Test and Biaxial Flexural Strength test were conducted to evaluate the mechanical properties of sintered nano-HAp and nano-TiO_2 specimens

3.6.5.1 Vickers Hardness Testing

To calculate the hardness of the nano-HAp samples Vickers Hardness Tester (Model LV-7000, LECO Co., St. Joseph, MI) was used. Load of 9.8 N was applied for 5 Sec. during the hardness test. By measuring the diagonals of the indent produced on the surface of the samples

hardness was calculated. There should be no crack propagation in the sample during the indentation. This is done to avoid any kind of error in the hardness measurement.

3.6.5.2 Biaxial Flexural Strength Measurement

Samples were tested in Ultimate Tensile Testing machine under compressive load (Model 3369, Instron Co, USA) with a constant crosshead speed of 0.02 mm/minute. For flexural test, ball piston (0.75 mm in diameter) was pressed against three hardened balls (1.98 mm in diameter) positioned 120^{o} apart in a circle of diameter 7.5 mm. Samples were centered on these three hardened balls Plastic sheet was placed between circular sample and ball piston to distribute the load evenly. Load at fracture was used to calculate biaxial strength using following equation.

$$S = -0.2387\ P\ (X-Y)/d2 \qquad \text{equation(5)}$$

Where

S - Maximum center tensile stress in MPa.

P - Load at failure in N.

$$X = (1+\nu)\ \ln (B/C)^2 + [(1-\nu)/2](B/C)^2 \qquad \text{equation(6)}$$

$$Y = (1+\nu)\ [1+ \ln (A/C)^2\ ]+ [(1-\nu)](A/C)^2 \qquad \text{equation(7)}$$

μ - poisons ratio

A - Radius of support circle in mm.

B - Radius of loaded area or ram tip in mm.

C - Radius of specimen in mm.

d - Thickness of the specimen at fracture origin in mm.

3.6.6 Assessment of Biomechanical Properties and Biodegradation

Simulated Body Fluid (SBF) was prepared on the basis of the recipe reported by T.Kokubo *et al*. [77] with an ion concentration nearly equal to that of human blood plasma. SBF was prepared in a plastic container without precipitation. pH of the SBF was maintained at 7.4. Biodegradation of the nano-HAp sintered samples was calculated by noticing their weight loss and decrease in strength in SBF as a function of time. Flow pattern was developed in SBF using magnetic stirrer.

Chemicals used in the preparation of SBF are:

1. Sodium chloride (NaCl)
2. Sodium hydrogen carbonate ($NaHCO_3$)
3. Potassium chloride (KCl)
4. Di-potassium hydrogen phosphate trihydrate ($K_2HPO_4.3H_2O$)
5. Magnesium chloride hexahydrate ($MgCl_2.6H_2O$)
6. Calcium chloride ($CaCl_2$)
7. Sodium sulphate (Na_2SO_4)
8. Tris-hydroxymethyl aminomethane
9. 1 N hydrochloric acid

1000 ml of SBF was prepared in a clean, scratch free plastic contained. Chemicals were dissolved in the sequence as shown above. Care was taken to add chemicals when the previous chemical was dissolved completely. Entire experiment was carried out in the temperature range of 34-38^oC with constant stirring.

3.7 Characterization of Sintered TiO_2 Structures

3.7.1 Biaxial Flexural Strength Measurement

Specimens were tested in Ultimate Tensile Testing machine under compressive load (Model 3369, Instron Co, USA) with a constant crosshead speed of 0.05 mm/minute and Biaxial flexural strength was calculated (as discussed in the above Section-3.6.5.2)

3.7.2 Assessment of Biomechanical Properties and Biodegradation

Simulated Body Fluid (SBF) was prepared on the basis of the recipe reported by T.Kokubo *et al*. [77] with an ion concentration nearly equal to that of human blood plasma (as discussed in above Section-3.6.6). Samples of HAp samples sintered at 1250^{o}C and TiO_2 samples sintered at 1400^{o}C and 1500^{o}C were placed in SBF for 28 days. SBF was maintained at pH of 7.4 throughout the experiment. At the end of every week samples were tested for their hardness, biaxial strength and mass loss.

4. RESULTS AND DISCUSSION

4.1 Nano-HAp Powder Characterization

4.1.1 Thermo-Gravimetric/Differential Thermal Analysis

Thermal stability of as synthesized nano-HAp was analyzed using Perkin Elmer TG-DTA (Pyris Diamond TG/DTA). TG-DTA was done to reveal the endo or exothermic reaction of the HAp sample which in turn was associated with the weight loss.

Nano-HAp powder was conditioned at 135^{o}C to remove moisture and organic impurities. After conditioning, sample was cooled to 45^{o}C and then heated to 1200^{o}C, in air, at a heating rate of 20^{o}C/min. During the experiment Helium gas flow rate was maintained at 160 cm^{3}/min.

As seen in the TG-DTA results presented in figure 6, with the increase in temperature weight-loss in the sample was observed. Total weight loss of 23% was calculated by the end of experiment at 1200^{o}C. This weight-loss can be contributed to the removal of adsorbed & possible lattice water, decarboxylation of HAp or condensation of HPO_4^{2-} releasing water [29]. Exothermic peak around 210^{o}C can be due to burning of some carbonaceous matter present in the HAp powder. Upon heating from 220-500^{o}C a mass loss of 9.6% is observed. This change of mass could be attributed to the partial removal of physically and chemically adsorbed water and possibly lattice water. All the endothermic peaks associated with mass loss below 600^{o}C can be contributed to desorption of adsorbed water and possible elimination of crystal lattice water. Endothermic peak around 600^{o}C and the corresponding significant weight-loss could possibly

because of decarboxylation and dehydroxylation of HAp releasing CO_2 and the condensation of HPO_4^{2-} releasing water [29].

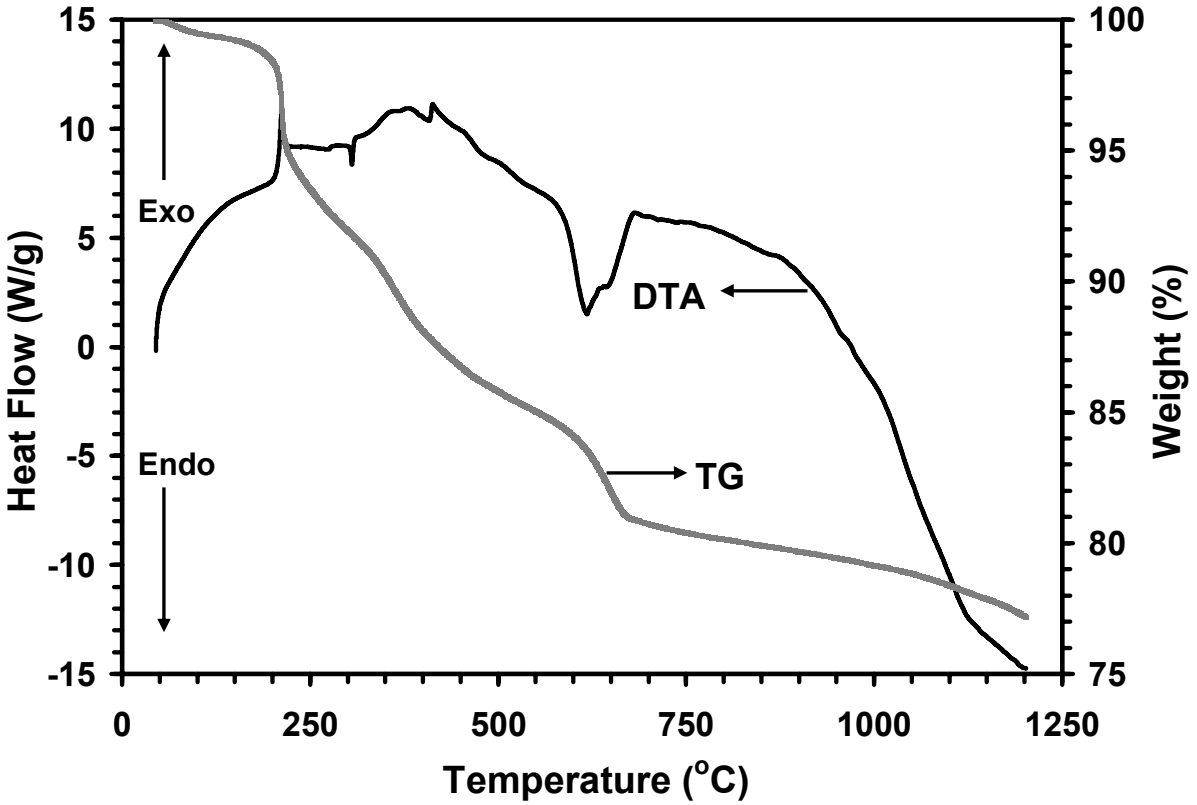

Figure 6: TG and DTA plot of as-synthesized nano-HAp

Wang *et al*. [78] discussed the dehydroxylation kinetics of HAp. Initially, dehydroxylation of HAp occurs due to OH^- anion diffusion through HAp and OH^- anion debonding from HAp lattice. HAp core size decreases with preceding dehydroxylation due to

which diffusion distance for OH^- anions through HAp becomes smaller. Oxyapatite [$(Ca_{10}(PO_4)_6O$] becomes stable as compared to HAp with increase in temperature. At this stage mass loss occurs due to oxyapatite lattice constitution. With further increase in temperature, dehydroxylation is controlled only by lattice constitution of oxyapatite by migration of O^{2-} anion in the OH^- depleted region. OH^- debonding and diffusion are too fast at high temperature to effect dehydroxylation rate. So in the final stage of dehydroxylation, oxyapatite lattice constitution and $2\ OH^- \rightarrow H_2O\uparrow + O^{2-}$ might be the rate controlling step.

Other researchers had reported much higher initial dehydroxylation temperature values (800^{o}C or higher) [79, 81]. A comparison of our results with TG-DTG curves reported by Wang *et al.* [78] shows that the onset of dehydroxylation of HAp is lower (570^{o}C) for our synthesized nanocrystalline powder compared to commercial HAp (Fluka brand, Signma-Aldrich Chemie GmbH, Germany). Such temperature discrepancy can also result from difference in powder synthesis methods and post-heat-treatments.

4.1.2 Phase Analysis and Crystallite Size Determination

X-ray diffraction patterns of the as-synthesized nanocrystalline hydroxyapatite powder are shown in figure 7. Plot (a) shows the pattern for dried powder after microwave synthesis, and plot (b) shows the pattern for calcined powder heat-treated at 500^{o}C after microwave synthesis.

Phase analysis was done using PDF card no. 00-009-0432 for Hydroxylapatite and PDF card no. 00-009-0169 for β-TCP, which provide information in the 2θ range of 10.820-78.229 degree. Phase analysis revealed that all major peaks of hydroxyapatite were present in both the powders. Energy given by the microwave radiation was sufficient to evolve major high intensity peaks of hydroxyapatite corresponding to various planes *viz.*, (111), (002), (211), (112), (300), (202), (301) and (310), as revealed by our analysis. As seen in plot (a), the peaks were broad for the dried powder obtained after microwave processing, which bring to light the smaller size of the crystallite/ particle in the powder.

To observe the effect of calcination, the powder was heat-treated at 500^{o}C and analyzed for phases. As seen in plot (b), calcination resulted in evolvement of new peaks and increase in peak intensity. This also led to some phase change marked by the unknown peaks as shown in the plot (b). Calcination increased crystallinity of the powder which is learnt from the increase in peak intensity corresponding to planes (200) and (210). Peak corresponding to plane (102) was also prominent in the calcined powder. However, calcination at 500^{o}C also coarsened the crystallite size in the powder as revealed by the narrower and sharper peaks compared to as-synthesized powder. Secondary phase of beta-tricalcium phosphate (β-TCP) was also observed in the nano-HAp powder calcined at 500^{o}C.

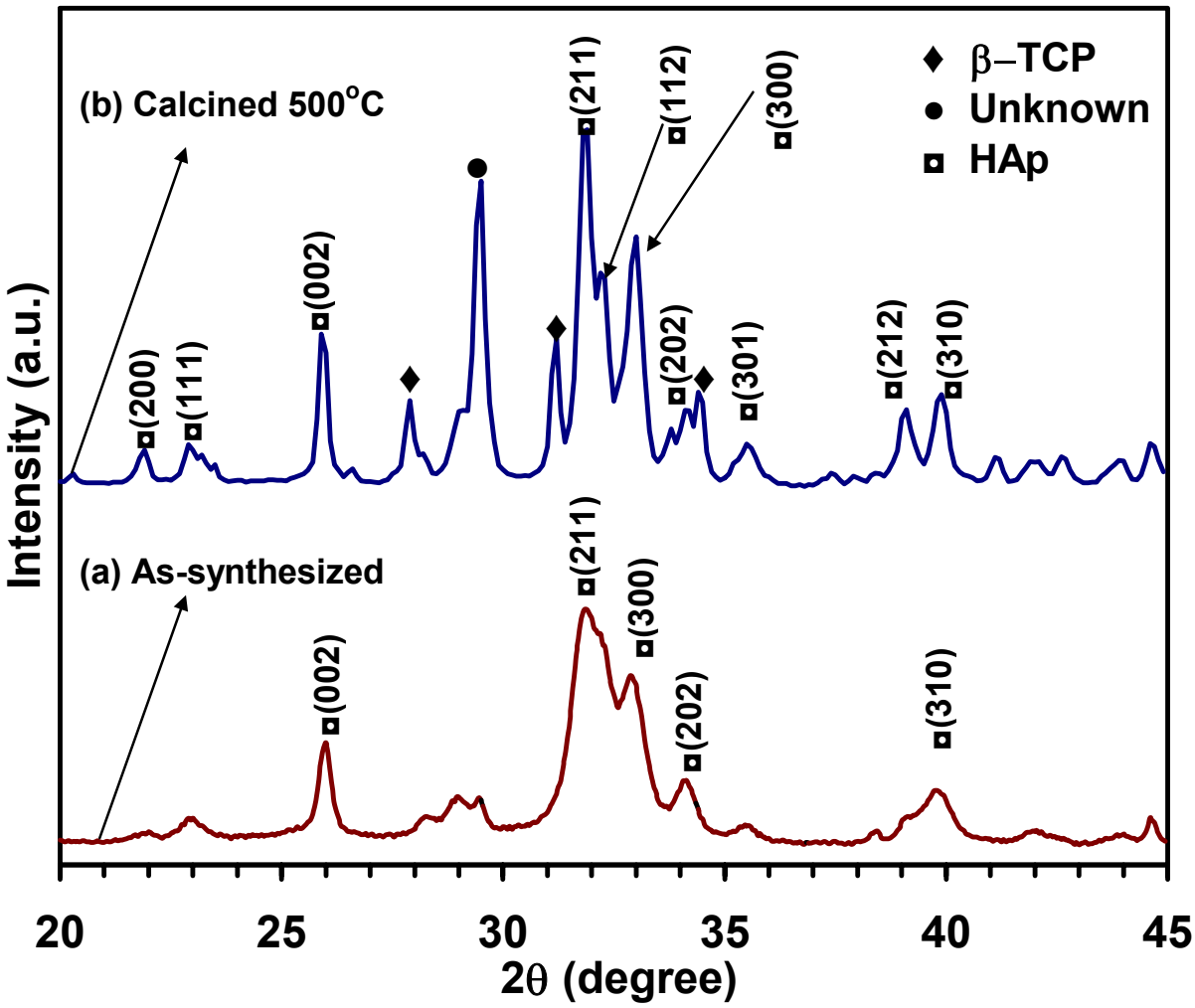

Figure 7: X-ray diffraction patterns of the as-synthesized nanocrystalline hydroxyapatite powder (a) Dried powder after microwave synthesis, and (b) Heat-treated powder at 500°C after microwave synthesis. Unknown peaks are marked as ●. Peak analysis was done using PDF card # 00-009-0432 and PDF card # 00-009-0169.

Crystallite size was calculated for two different value of θ for as-synthesized and calcined HAp powder by using Scherrer's formula as shown in Table 6:

$$B_{crystallite} = k\lambda/L\cos\theta \qquad \text{equation(8)}$$

where k is a constant (usually 0.9), λ is the wavelength of X-ray radiation, L is the average particle size, and θ is the Bragg angle, crystallite size was calculated for as-synthesized and calcined HAp powder.

Table 6: Comparison of the crystallite size calculated using Scherrer's formula for As-synthesized and Calcined nano-HAp for different 2 θ values.

2 θ	**Crystallite Size (nm)**	
	As-synthesized Powder	**Calcined Powder at 500^{o}C**
25.9	14.13	21.46
31.8	11.29	16.58

Where λ=1.5418 Å, k=0.9

The crystallite size of the as-synthesized HAp crystals was in the range of 11-15 nm.

Manjubala *et al*. [82] discussed the synthesis of biphasic calcium phosphate ceramics using microwave radiation. It was observed that biphasic calcium phosphate powders prepared with the different Ca/P ratio was accountable for different volume fraction of β-TCP formed. When molar concentration of calcium to phosphorus solution used was less than 1.67, peaks of β-TCP were observed in the as-synthesized and calcined powder.

Yang *et al*. [32] discussed the thermal stability of HAp derived from the microwave irradiation method. It was observed that sample irradiated for 5 min at 700 W had Ca/P molar

ratio of 1.54 and sample irradiated for 30 min at 700 W have Ca/P molar ratio of 1.63. Well crystallized HAp and β-TCP peaks were observed in the samples irradiated for 30 min at 1000^{o}C whereas samples irradiated for 1h showed well crystallized peaks of HAp only.

HAp is decomposed at higher temperature as follows:

$$Ca_{10}(PO_4)_6(OH)_2 \rightarrow 3Ca_3(PO_4)_2 + CaO + H_2O$$

But with the increase in irradiation time, thermal stability of HAp increases [32]. Generally, in short irradiation time calcium deficient HAp was formed which is responsible for different thermal stability. HAp prepared in a short irradiation time is thermodynamically metastable phase which transform to relatively stable phase at elevated temperature.

4.1.3 Powder Morphology, Agglomeration and Particle Size Determination

4.1.3.1 Transmission Electron Microscopy

Figure 8 shows the high-resolution TEM micrograph of the as-synthesized nano- HAp crystallites via microwave processing without calcination. From these TEM micrographs, it can be seen that the powder was needle shaped with diameter of ~ 5-10 nm and length of 15-30 nm.

High resolution TEM micrograph of the as-synthesized hydroxyapatite nano-powder is shown in figure 9. It shows clear lattice fringes, indicating the established crystallinity of HAp powder. Since a crystallite can be defined by studying the orientation of the lattice fringes, one can see the average grain size in the synthesized HAp powder is about ~10-20 nm, which is in good agreement with the calculated value calculated using Scherrer's formula from XRD phase analysis. Also, we know that the lattice images are interference patterns between the direct beam and diffracted beams in HR-TEM and the spacing of a set of fringes is proportional to the lattice spacing, when the corresponding lattice planes meet the Bragg condition.

Figure 10 shows the EDS spectrum and powder diffraction pattern of the as-synthesized powder soon after microwave synthesis. The EDS spectrum confirms its chemical composition and powder diffraction pattern further validate the crystallinity of the powder. Clear peaks corresponding to Ca, P and O can be seen in the EDS spectrum.

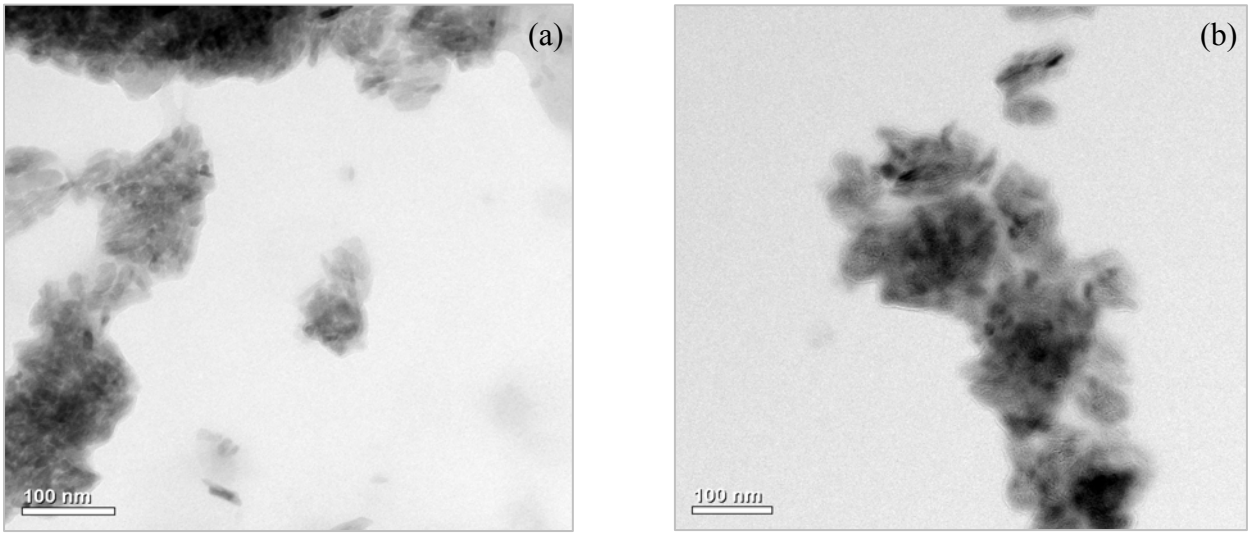

Figure 8: TEM micrograph of the as-synthesized nano-HAp powder. (a) Micrograph showing extremely fine individual nano-HAp powder (10-50 nm) with loose agglomeration, and (b) micrograph exhibiting large agglomerates of HAp nanopowder.

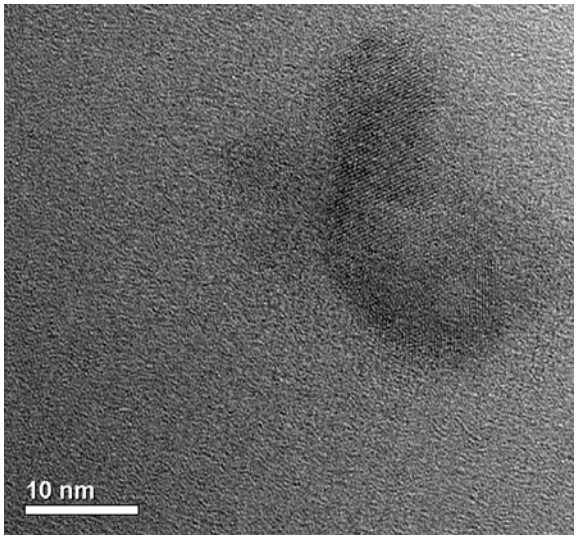

Figure 9: High resolution TEM micrograph of HAp nano powder showing crystallographic planes. Grain size can be approximated to be 10-20 nm.

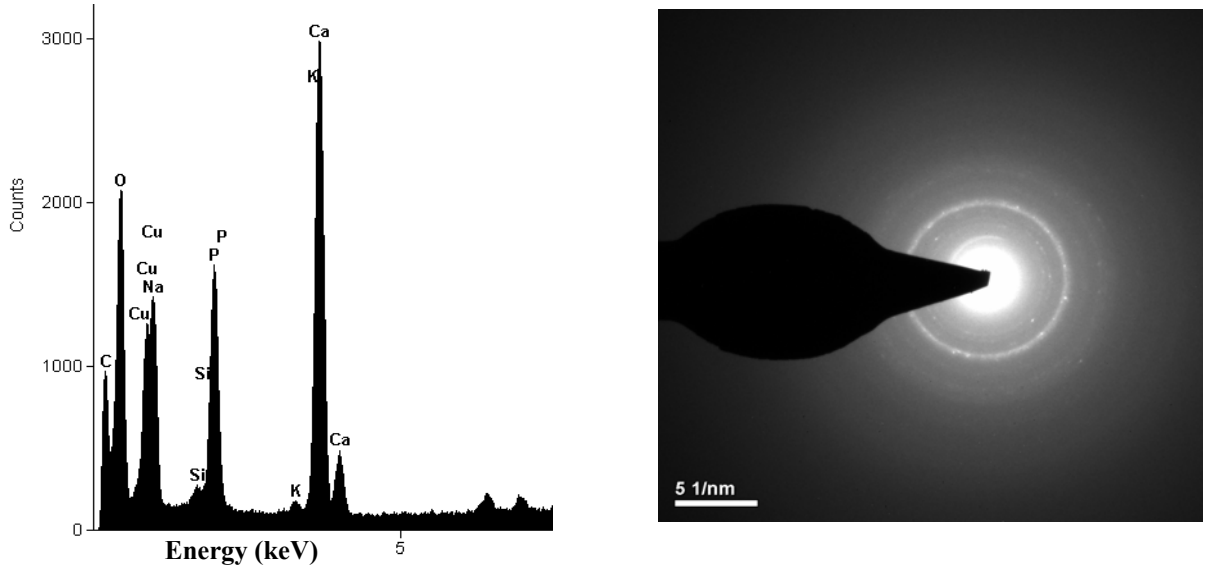

Figure 10: (a) EDS spectrum, and (b) powder diffraction pattern of the as-synthesized (as-synthesized) nano-phase powder confirming its chemical composition and crystallinity, respectively.

Siddharthan *et al*. [28] studied the influence of microwave power on nano-HAp particles. It was observed that lower power of 175 W resulted in crystals with needle-like shape because microwaves absorption by free and bound water is less resulting in few HAp nuclei and growth taking place at slow rate at low temperature. HAp morphology also change to acicular shape for 525 W and platelet shape for 660 W. Due to limitation of crystal growth in c-direction morphology of the crystal changes occurs.

4.1.3.2 IQ Materials Image Analysis: Particle size measurement

Particle size was measured on SEM image shown in Figure 11 using IQ Materials Image Analysis software. The Particle Size module of IQ materials Image Analysis software automatically detects and measures particles pictured in captured images. This software makes its initial measurements in terms of pixels. The calibration was done to converts these to more meaningful units, such as millimeters, micrometers etc for the image under analysis. Specific area of interest in image can be analyzed using this software. The more image data that you analyze, the more accurate your results will be.

This module provides valuable information regarding measurable characteristics of particles, including:

- Size measurements (for example, perimeter, length, width, and area)
- Location information (X-Y coordinates)
- Easy thresholding tools for identifying particles of interest in images.
- Shape and orientation measurements (for eg, degree of circularity and angle of rotation).
- Ability to control particle recognition by setting a minimum size requirement.
- Summary statistics on all measurements.

Figure 11 presents the scanning electron micrographs of simply dried HAp nano powder after microwave synthesis which was captured at 12000 X with an acceleration voltage of 5 kV. SEM observation of the powder reveals that the powder was a loose agglomerate of very fine particles and these particles are in the nano regime (10-25 nm as can be clearly seen in the figure 11a). The size of agglomerates varied between 50 nm to 4 μm. Figure 11(b) shows the analyzed particles of HAp in blue color with green periphery around it. Results of particle size (surface

area) analysis of synthesized HAp powder from SEM micrograph (figure 11(b)) using IQ Materials Image Analysis software are shown in figure 11(a). In this colored particle surface area analysis, the blue color area surrounded by green represents particle and agglomerate observed in SEM image. The plot of number of particles as a function of particle surface area clearly shows that the majority of the particles is very fine and is in the range of 10-50 nm.

Histogram was plotted on the basis of the analyzed particles as shown in Figure 12. Number of particle in the nano-range can be easily calculated from the histogram. It was observed that majority of the particles were in the range of 10-50 nm which has already been confirmed by XRD plot and TEM micrograph of the as-synthesized HAp. Loose agglomerates of HAp nano-particles in the range of 0.5-1.0 μm were observed in the SEM image analyzed by IQ materials image analysis software.

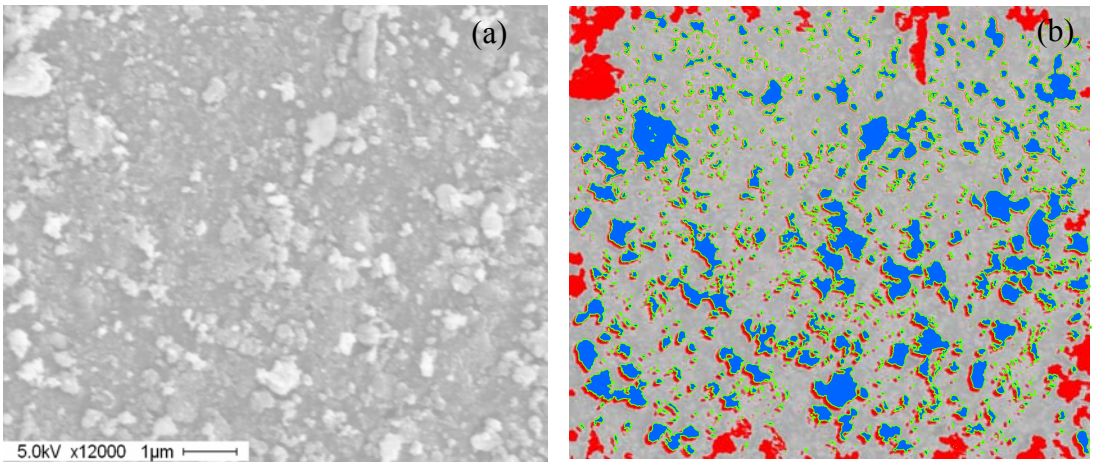

Figure 11: SEM micrographs of the as-synthesized hydroxyapatite nano-powder (a) high magnification micrograph showing individual HAp particles in the nano-range (10 – 50 nm), and 1(b) Analyzed SEM image for particle size measurement using IQ materials image analysis software.

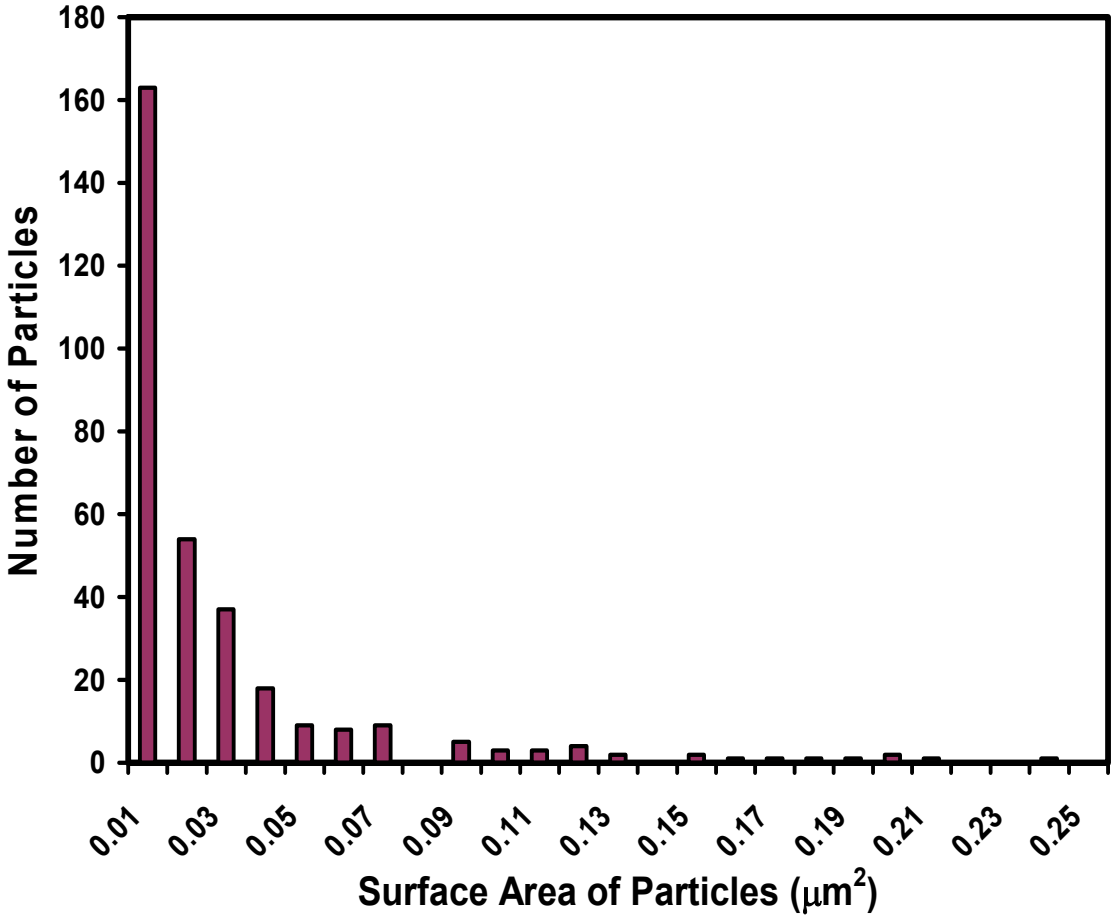

Figure 12: Histogram of particle size measurement on the SEM micrograph of HAp using IQ Materials Image Analysis software. Majority of the particles were in the range of 10-50 nm.

Meejoo *et al*. [29] performed Dynamic Light Scattering (DLS) on the as-synthesized nano-HAp precipitate to calculate the particle size distribution. DLS analysis gave an insight that particle size distribution of the precipitate was in the range of 28-153 nm.

Table 7: Summary of the recent research work in synthesis of nano HAp powder using microwave radiation

Researchers	**Powder Morphology**	**Phase composition**	**Power used**	**Crystallite Size**
Siddharthan *et al.* (2006) [28]	Platelet	HAp	660W	32-42 nm
Parhi *et al*. (2004) [30]	Spherical	HAp		~100 nm
Rameshbabu *et al*. (2005) [86]	Plate like	HAp	800W	W=15-20 nm L=60-80 nm
Meejoo *et al*. (2006) [29]	Needle shape	HAp	850W	D=50 nm L=100 nm
Manjubala *et al*. (2001) [82]		HAp+β-TCP	800W	
Han *et al*. (2006) [31]	Needle and Spherical	HAp	550W	W=4-15 nm L=20-50 nm and D=10-30 nm
Siddharthan *et al*.(2005) [87]	Needle like	Calcium deficient HAp	800W	L=16-39 nm W+7-16 nm
Our work	Rod like	HAp+ β-TCP	600W	10-15 nm

4.2 Sintering and Densification Study

4.2.1 Density Measurement of HAp structures

Uniaxially compacted HAp pellets at a pressure of 78.69 MPa were sintered at 1100^{o}C, 1150^{o}C, 1200^{o}C, 1250^{o}C with holding time of 4.5 h in programmable high temperature muffle furnace. Geometric bulk density (ρ_g) of the sintered specimens was evaluated from the measurements of the mass of specimen and its volume (determined by dimensional measurements) using equation (9).

Geometric bulk density (ρ_g) = Mass (m) / Volume (V) equation (9)

Effect of sintering temperature on the bulk density of nano-HAp is shown in Figure 13. Average sintered density computed for the same set of specimens increased from 2.50 g/cc (±0.06) at 1100^{o}C to 2.88 g/cc (±0.03) at 1250^{o}C which is 93.5% of the theoretical weight of HAp. It can be noticed from the plot that the densification process continued with the elevation in temperature which is in agreement with what is reported in the literature [83, 85]

Pattanayak *et al*. [83] studied the effect of sintering temperature on HAp samples compacted at 700MPa. Sintered density of 2.7 g/cc was obtained at 1200^{o}C whereas in our research, density of 2.8 g/cc was achieved at 1200^{o}C for the samples compacted at a pressure 9 times less than the compaction pressure used above.

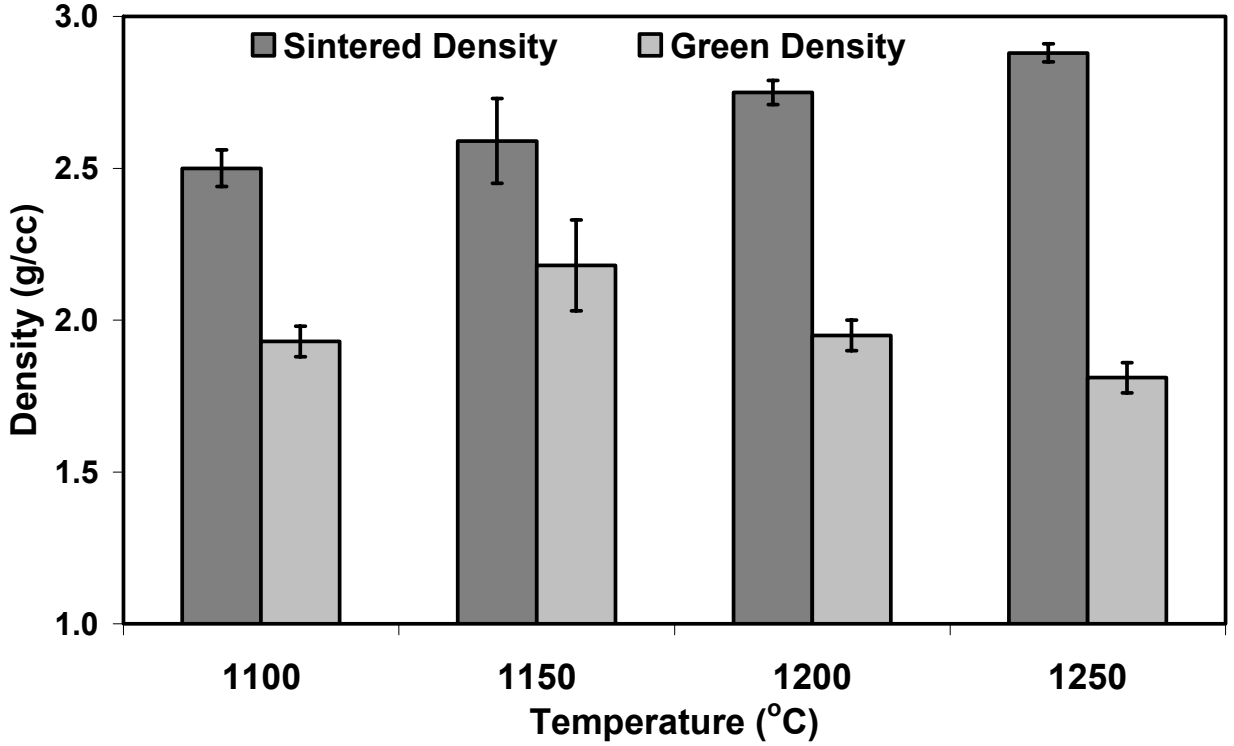

Figure 13: Sintered density of HAp structure as a funtion of sintering temperature.

4.2.2 Density Measurement of TiO_2 structures

Uniaxially compacted TiO_2 samples were sintered at 1400°C and 1500°C. Not much change in the density was observed with increase in temperature from 1400°C to 1500°C. Average sintered density computed for the same set of specimens increased from 3.77 g/cc (±0.11) at 1400°C to 3.84 g/cc (±0.04) at 1500°C. At 1500°C, 98% of the theoretical density of TiO_2 was achieved. With the increase in temperature, porosity decreases resulting in better densification at the expense of grain growth.

4.2.3 Phase Analysis of Sintered Structures

4.2.3.1 Phase Transformation in HAp

X-ray powder diffraction analysis was conducted to analyze phase transformation in HAp structures sintered at different temperatures that is, 950^{o}C, 1100^{o}C, and 1200^{o}C, separately. Results of phase analysis are presented in figure 14. Peaks in each X-ray diffraction pattern were recorded and verified using PDF card # 00-029-1193 for $NaCaPO_4$ and PDF card # 00-011-0236 for $Na_3Ca_6(PO_4)_5$. Intensity and sharpness of the peaks grew with the increase in sintering temperature, indicating an increase in the crystallite size in the sintered structures as the sintering temperature was raised from 950-1200^{o}C. In addition to HAp, $NaCaPO_4$ and $Na_3Ca_6(PO_4)_5$ were also observed at 950^{o}C, 1100^{o}C and 1200^{o}C. New phases of sodium calcium phosphate appeared due to the presence of sodium in the system which was confirmed from EDS spectrum.

Jalota *et al*. [33] synthesized biphasic material of β-$NaCaPO_4$ and HAp for skeletal repair. β-$NaCaPO_4$ and HAp peaks were observed in CaP gel precursor calcined at 600^{o}C. β-$NaCaPO_4$ phase transforms to α-$NaCaPO_4$ at 650^{o}C which is isostructural with β-K_2SO_4

HAp posses high biocompatibility and new bone grows directly on the implant without fibrous encapsulation. $NaCaPO_4$ can be used to develop osteoinductive or bioresorbable calcium phosphate bioceramics because rate of bone growth on $NaCaPO_4$ sample surface is much more than that of HAp [42]. Nikahira *et al.* [47] did SBF study on HAp samples containing $NaCaPO_4$ sintered at 1000^{o}C by placing the samples in SBF for 4-7 days. HAp samples containing $NaCaPO_4$ showed higher bioactivity than pure HAp. $Na_3Ca_6(PO_4)_5$ is a new bioceramic on which research is still going on. Bioactivity of $Na_3Ca_6(PO_4)_5$ is much more than HAp [49] and it was

also noticed that cement with sodium calcium phosphate ($Na_3Ca_6(PO_4)_5$) when mixed with malic acid or citric acid was far less toxic than the commercial carboxylate cement used as negative control in He-La cell culture [46].

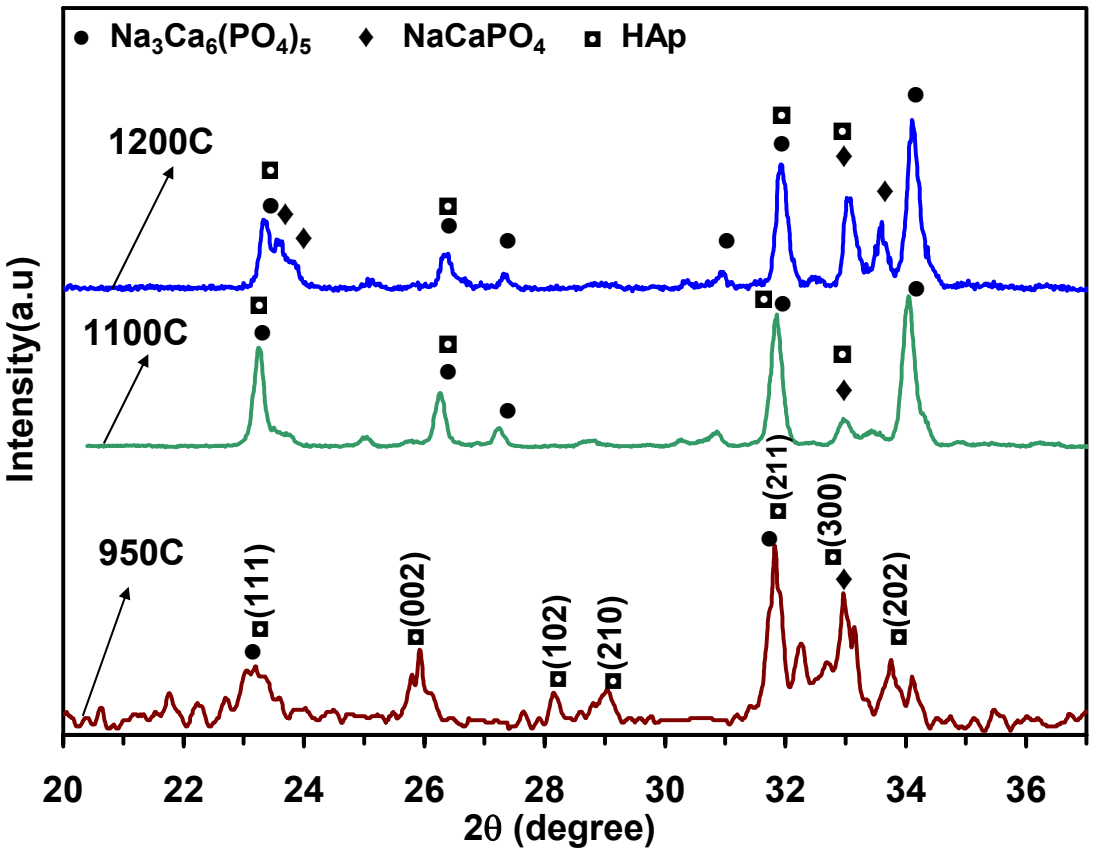

Figure 14: Phase analysis of nanostructured HAp ceramics as a function of sintering temperature. Specimens were sintered in air at 950°C, 1100°C, 1200°C for 4.5 h separately, in a muffle furnace.

4.2.3.2Phase Transformation in TiO_2

The XRD patterns for nano-TiO_2 powders calcined at 400°C, sintered at 1400°C and 1500°C for 3 h, are shown in Figure15. Presence of rutile phases of TiO_2 was confirmed by

comparing with JCPDS standard files #21-1276, respectively. No phase change was observed between 1400°C and 1500°C but increase in intensity and the sharpness of the rutile peaks was observed with increase in sintering temperature, demonstrating increase in crystallite size.

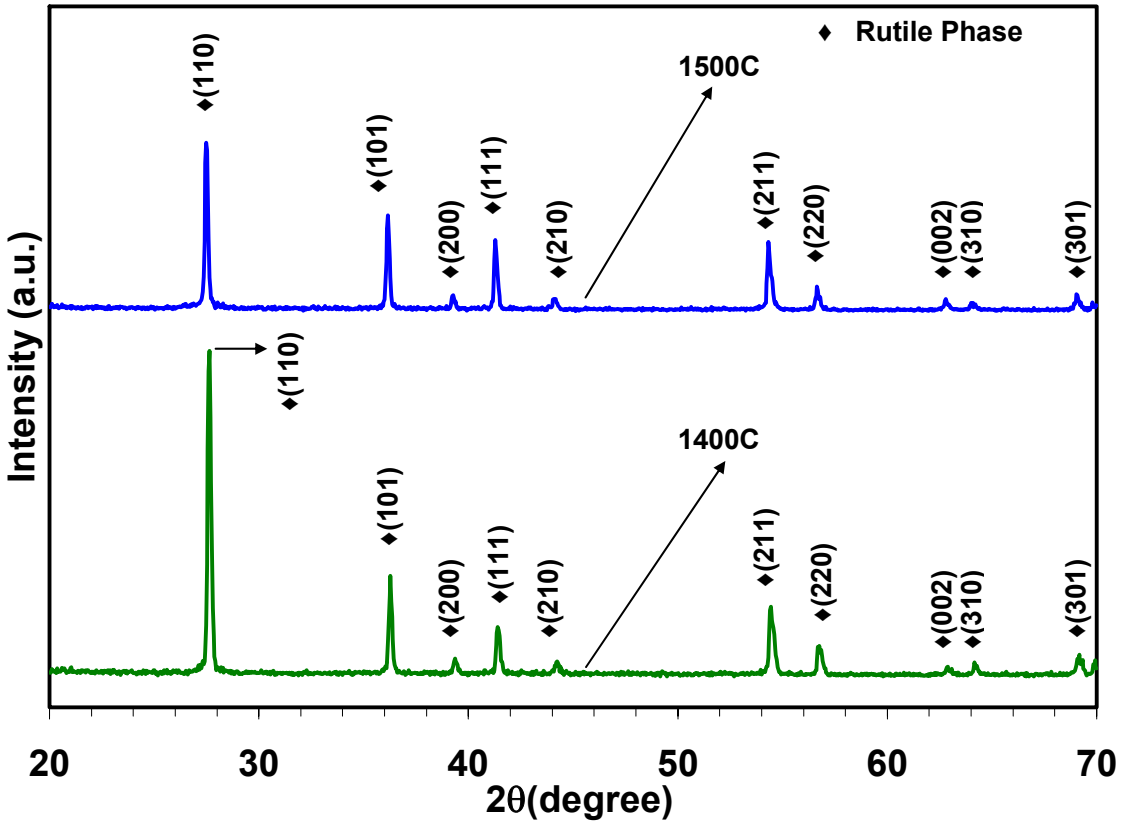

Figure 15: X-Ray diffraction pattern of TiO_2 powder heat-treated at 1400°C and 1500°C. Peaks were analysed using JCPDS standard files # 21-1276.

4.2.4 Microstructure Analysis

4.2.4.1 IQ Materials Image Analysis-Grain size measurement

HAp grain size measurement

The Grain Size module of IQ materials software was used to obtain ASTM E 112 grain size value for grains depicted in captured Image. Grain Size module automates the grain boundary intercept method of grain size determination by auto-detecting grain boundaries intercepted by virtual lines drawn across the image. Then, it calculates the ASTM E 112 grain size value based on the grain boundaries intercepted.

Some features of grain size module of IQ materials software:

- Simple and effective grain boundary definition process
- Ability to choose the best intercept method for your purposes, including circle, horizontal, vertical, and diagonal methods
- Ability to control grain boundary recognition through thresholding and pattern matching options
- Ability to manually add and remove boundary intercepts that are missed by the auto-detection function
- Grain boundary reconstruction and special handling of twin grain boundaries

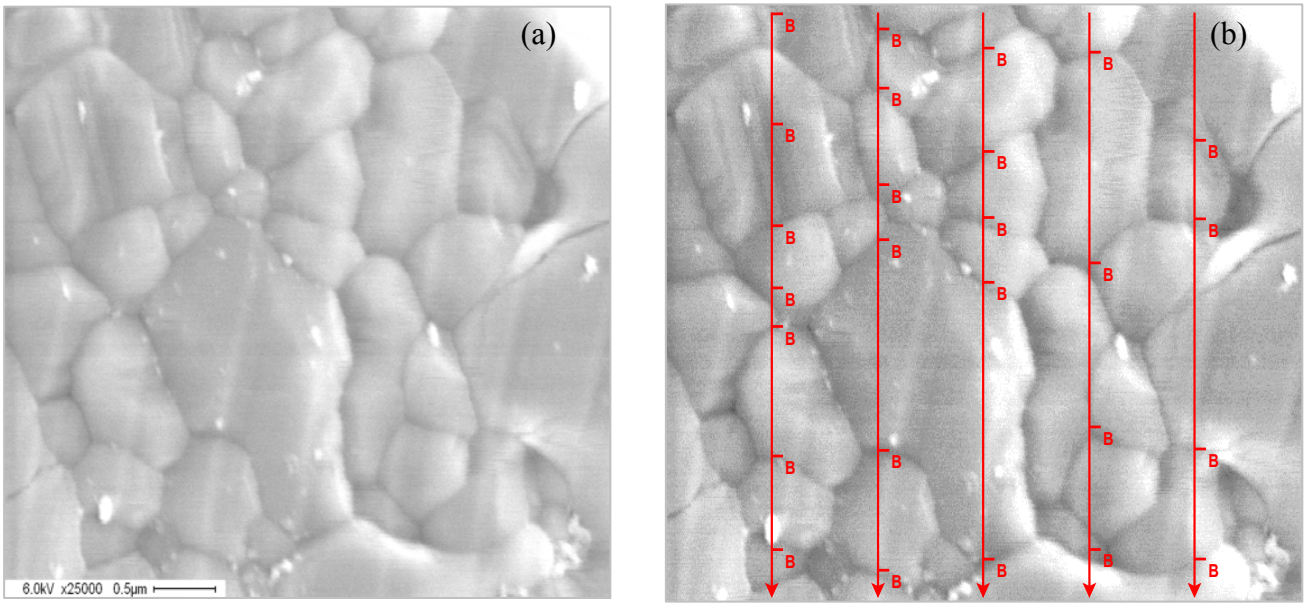

Figure 16: SEM micrographs of the sintered hydroxyapatite structure for grain size measurement (a) high magnification micrograph showing grain size of HAp sample sintered at 1150^{o}C for 4.5hr, and 1(b) Analyzed SEM image for grain size measurement using IQ materials image analysis software.

Grain size was measured using Grain size module of IQ material software on the SEM image of HAp as shown in Figure 16(b). Grain Size module automates the grain boundary intercept method of grain size determination by auto-detecting grain boundaries intercepted by virtual lines drawn across the image. It was observed that ASTM grain size (Number of grains per square inch at a magnification of 100 X) was 14 for sintered HAp at 1150^{o}C.

Meejoo *et al*. [29] observed that at a sintering temperature of 900^{o}C grain size of nano-HAp tripled and particles started joining their neighbor for the incremental growth process. At 1200^{o}C, noticeable grain growth was observed and nano-HAp samples with grain size of 1µm in diameter were obtained.

4.2.4.2 IQ Materials Image Analysis - Porosity measurement

Percent Area module of IQ materials software determine the percentage of area covered by particular phases pictured in captured images. It automatically detects and measures the area of particles pictured in captured images. Following the ASTM E1245 Standard, this module determines the percentage of area in an image that is covered by different particular phases of material.

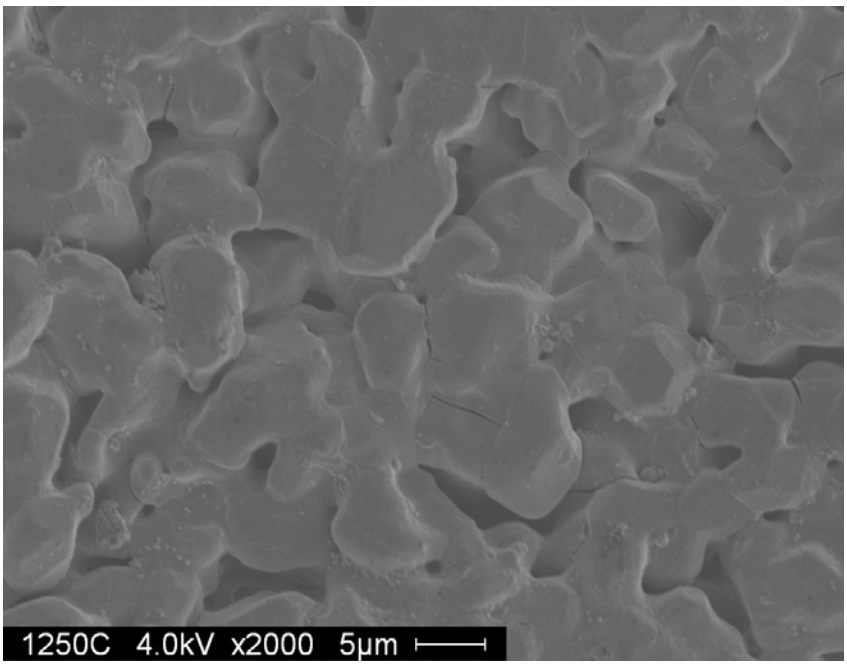

Figure 17: SEM micrographs of the hydroxyapatite structure sintered at 1150^{o}C for 4.5h for porosity measurement.

Porosity was measured on the SEM micrograph shown in Figure 17 using Percent area module of IQ materials software. The measured percentage porosity value of HAp samples pressed at 78.69 MPa and sintered at 1250^{o}C for 4.5 h was 4.04 ± 0.49%.

4.2.5 Fourier Transform Infrared Spectroscopy

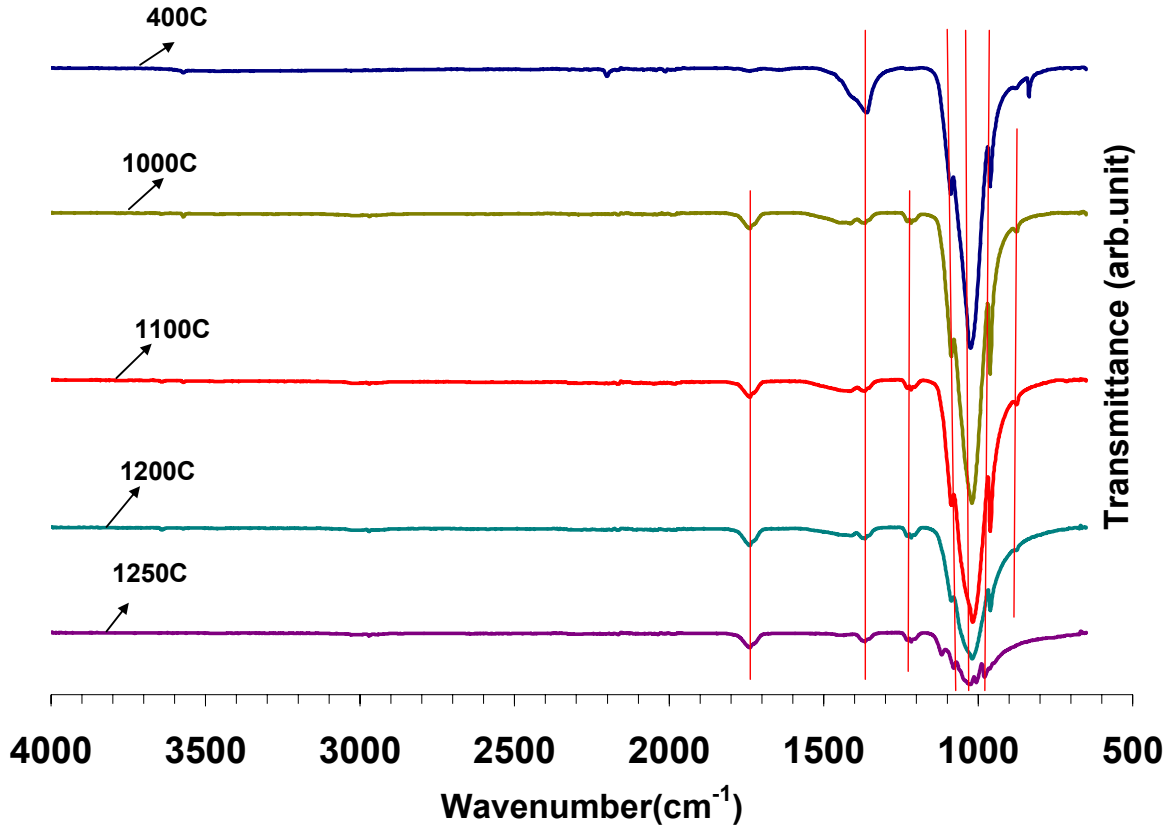

Figure 18: FTIR spectrum of HAp at 400°C, 1000°C, 1100°C, 1150°C, 1200°C, and 1250°C.

Nano-HAp powders were analyzed using Perkin Elmer 100 spectrum FT-IR Spectrometer in the wave number region 650-4000 cm^{-1} to distinguish the type of calcium phosphate. The samples were finely powdered prior to the measurement. The baseline of the whole spectrum was corrected prior to the spectra of the powder samples. Fig18 show the IR spectra of nano-HAP precipitate sintered at different temperature varying from 400-1250°C. All IR spectra in this study were compared with the earlier experiments performed in this direction [29, 82]. IR spectra conformed that the nano-HAp is of typical apatite structure. Hydroxyl and Phosphate group in the apatite structure can be substituted by carbonate, fluoride or chloride.

From literature, [82-84] characteristic IR peak around 873 cm^{-1} can be due to the substitution of phosphate site by carbonate ions in apatite. It was found that with the increase in temperature carbonate ions are removed from the apatite structure and OH^- peak around 3570 cm^{-1} becomes narrower and then disappears [82]. Intensity of peaks corresponding to Carbonate and Hydroxyl groups changes significantly with the increase in temperature. Because of condensation of $2HPO_4^{2-}$ to $P_2O_7^{4-}$ intensity of HPO^{4-} band decreases over the range of 870-840 cm^{-1} [84]. The band around 1000 cm^{-1} appears as triplet in pure HAp with peaks well resolved at 1096, 1085 and 1056 cm^{-1}, but in Biphasic Calcium Phosphate (BCP) samples the triplet resolution decreases and broadening takes place [82]. The carbonate vibrational bands in the region 1650-1300 cm^{-1} are assigned to the surface carbonate ions due to the air atmosphere present during the processing and characterization.

Pattanayak *et al*. [83] (2005) synthesized and evaluated the HAp ceramics. In the FTIR analysis conducted phosphate was characterized by a strong, complex band in the 1000-1150 cm^{-1} range, and, a medium intensity band at about 960 cm^{-1}. In the FTIR spectrum obtained in this study a peak can be observed at 1086.35 cm^{-1} at 1200^oC. Also the peak observed at 3571.2 cm^{-1} corresponds to characteristic OH^- band. The OH peaks become narrower as temperature is increased from 400^oC to 1000^oC, indicating the removal of some amount of hydroxyl component such as water from crystalline structure. After heat treatment at 1000 degrees, the OH absorption band disappeared. The peak at 1738.79 cm^{-1} confirmed the existence of a Ca-O phase in the structure. Also it can be observed that there are significant changes in intensity and appearance of peaks corresponding to carbonate and hydroxyl groups.

4.3 Mechanical Characterization

4.3.1 Vickers Hardness Measurement

4.3.1.1 Nanostructured HAp

HAp powder calcined at 400^{o}C was pressed into pellets at a pressure of 78.69 MPa and sintered at high temperature to study the effect of sintering temperature on hardness. Figure 19 gives the Vickers hardness number observed for nano-HAp samples sintered in the range of 1100-1250^{o}C.

It can be noticed that Vickers hardness number increased with the increase in sintering temperature, and a maximum hardness value of 249.53 ± 3.98 HV (2.44 ± 0.04 GPa) was observed for samples sintered at 1250^{o}C. Observed hardness value can be well correlated with the sintered density, that is, when sintered density is low, corresponding hardness value is also low. For instance, samples sintered at 1100^{o}C had an average bulk density of 2.50 ± 0.06 g/cc and their average hardness was only 118.86 ± 7.17 HV. Whereas, a maximum hardness value of 249.53 ± 3.98 HV was achieved for the samples sintered at 1250^{o}C having highest geometrical bulk density of 2.88 g/cc (±0.03). Increase in densification may be attributed to the decrease in porosity of samples with the increase in temperature at the expense of grain growth.

Ramesh *et al*. [85] achieved Vickers hardness of 6.38 (±0.30) GPa for the HAp samples microwave sintered at 1150^{o}C. Microwave sintering helps in suppressing the grain coarsening that is normally inevitable in conventional sintering.

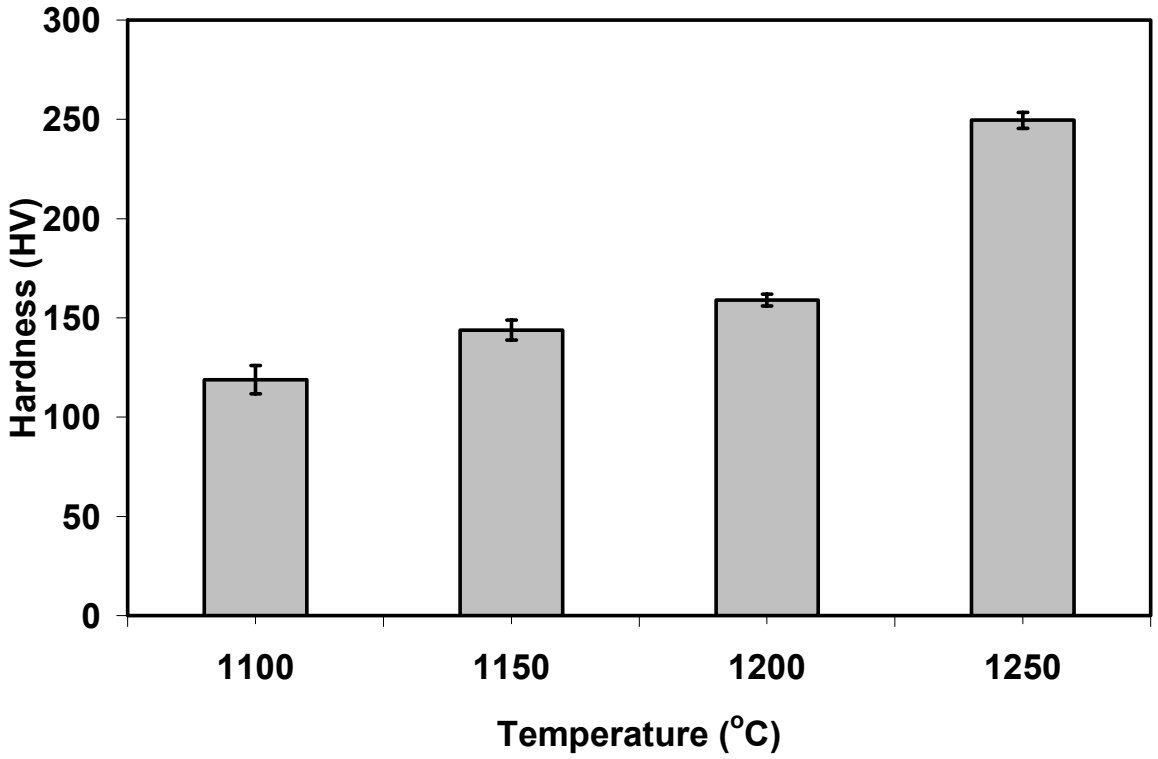

Figure 19: Variation in Vicker's Hardness of HAp structures as a function of sintering temperature.

4.3.1.2 Nanostructured TiO_2

Nano-TiO_2 powder calcined at 400°C was pressed into pellets at a pressure of 78.69 MPa and sintered at high temperature to study the effect of sintering temperature on hardness. It can be noticed that Vickers hardness number increased with the increase in sintering temperature. Hardness of 637.03 ± 6.90 HV was achieved for the samples sintered at 1400°C whereas samples sintered at 1500°C were having little higher hardness of 643.27 ± 7.96 HV. Maximum hardness value of 643.27 ± 7.96 HV was achieved for the samples sintered at 1500°C having highest geometrical bulk density of 3.84 g/cc (±0.04).

4.3.2 Biaxial Flexural Strength Measurement

4.3.2.1 Nanostructured HAp

HAp powder calcined at 200^{o}C was pressed into pellets and sintered at high temperature to study the effect of temperature on biaxial strength. Biaxial flexural strength was calculated for at least six sintered specimens and it was observed that biaxial flexural strength increased with the increase in temperature. Maximum biaxial flexural strength of 52.07 ± 4.96 MPa was observed for the sample sintered at 1250^{o}C. Percent porosity of the HAp samples sintered at 1250^{o}C for 4.5 h was measured using Percent area module of IQ materials software as shown in Figure 17. Low porosity of 4.04 ± 0.49% was observed which may be responsible for the increase in biaxial strength of the HAp sample.

Pattanayak *et al*. [83] observed that biaxial flexural strength is higher for the samples sintered at 1100^{o}C (50MPa) as compared to the samples sintered at 1150^{o}C and 1200^{o}C. This happens due to the presence of excess of Tricalcium phosphate/Dicalcium Phosphate strength of apatite above 1100^{o}C.

Thangamani *et al*. [88] synthesized nano-HAp using precipitation reaction. HAp samples sintered at 1100^{o}C showed a maximum flexural strength value of 42.6 ± 6 MPa and with the increase in sintering temperature, decrease in strength was observed. Decrease in strength can be attributed to the abnormal and inhomogeneous growth of grain above 1100^{o}C.

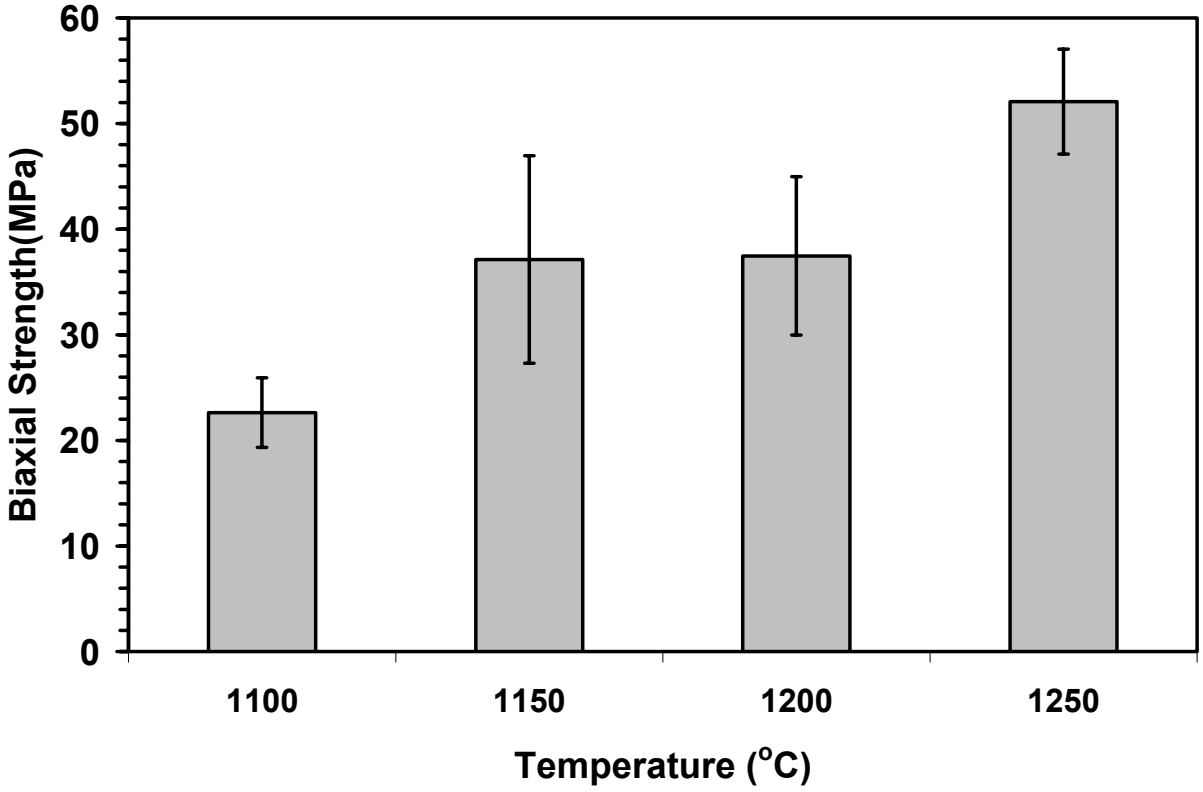

Figure 20: Variation in Biaxial Flexural Strength of HAp structures with varying sintering temperature.

4.3.2.2 Nanostructured TiO_2

TiO_2 powder calcined at 400°C for 3 h was pressed at a pressure of 78.69 MPa and sintered to study the effect of temperature on biaxial strength. It was observed that the calculated biaxial strength increased with increase in temperature. Biaxial flexural strength of 118.94 ± 6.17 MPa at 1400°C and 125.5 ± 5.76 MPa was observed for the samples sintered at 1500°C.

4.4 Biomechanical Property and Biodegradation in Simulated Body Fluid

4.4.1 HAp structures

Twelve HAp samples sintered at 1250^{o}C were studied for their bioactivity and biodegradability by placing the samples in Simulated Body Fluid (SBF) for 21days as shown in Figure 21. pH of the SBF was maintained at 7.4 and was stirred throughout the experiment. At the end of every week 4 samples were taken out of SBF and observed for their change in mechanical properties. It was observed that the hardness of the sintered HAp samples decreased with time in SBF. Final hardness of 130.2 ± 2.68 HV on 21st day was achieved as compared to the initial hardness of 249.53 ± 3.98 HV on day zero. Maximum biaxial strength of 55.07 ± 12.41 MPa was achieved on the 21st day.

Figure 21: Experimental setup for biodegradability study of HAp sample sintered at 1250^{o}C.

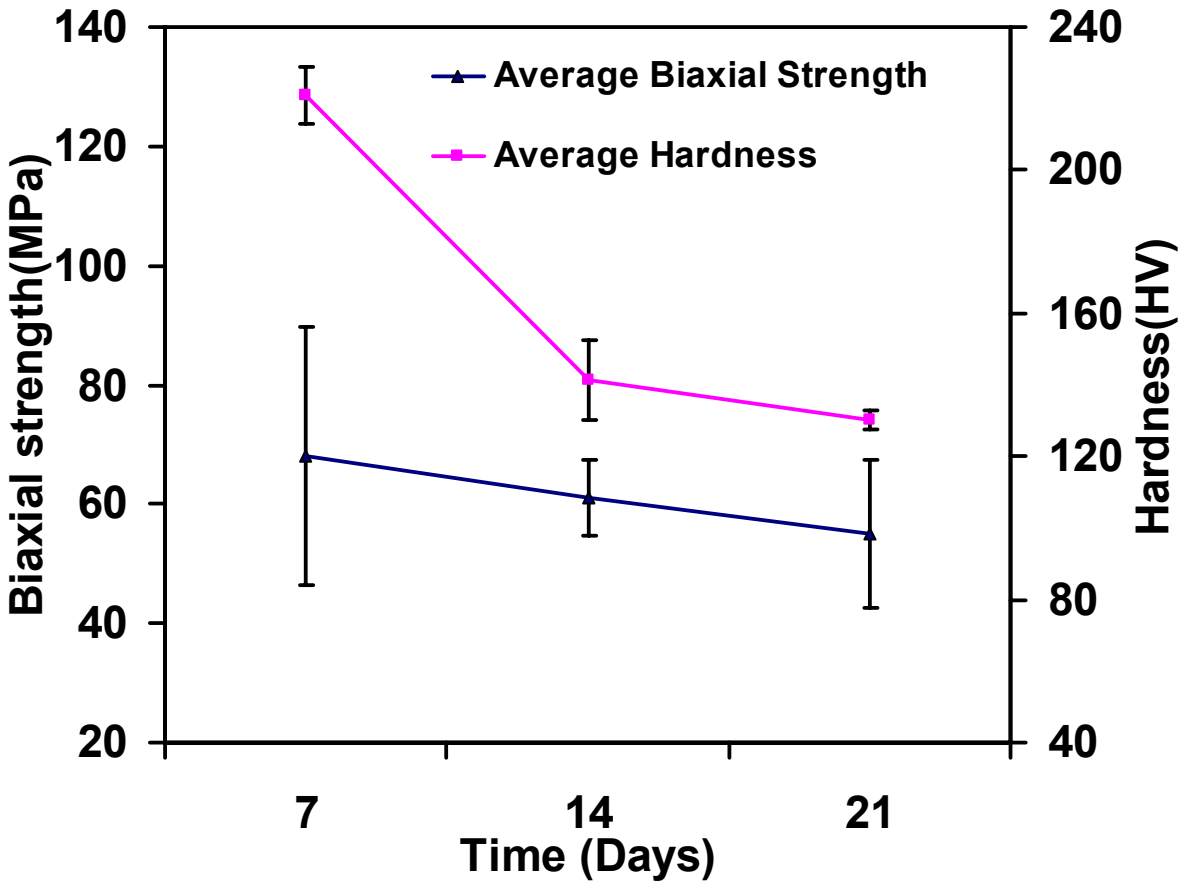

Figure 22: Variation in Biaxial flexural strength and Hardness of sintered HAp (1250^{o}C) in SBF.

4.4.2 TiO_2 structures

Biodegradation study was done on 8 TiO_2 samples sintered at 1400^{o}C. Samples were placed in a small box having number of holes. This small box was placed in SBF for 28 days as shown in Figure 23. To maintain the pH of SBF at 7.4, SBF was replaced biweekly. SBF was stirred during the entire experiment. At the end of every week, two TiO_2 samples were taken out of SBF to study their mechanical properties. It was observed that hardness of TiO_2 samples

sintered at 1400°C decreases with time in SBF and hardness of 293.20 ± 8.45 HV was obtained on 28th day as compared to the initial hardness of 637.03 ± 6.90 HV on day zero. TiO_2 samples sintered at 1400°C were further tested for their biaxial strength. It was also observed that biaxial strength followed the same decreasing trend as followed by hardness. Biaxial strength of 104.29 ± 1.84 MPa was achieved on 28th day as compared to the initial biaxial strength of 118.94 ± 6.17 MPa on day zero.

Figure 23: Experimental setup for biodegradability study of TiO_2 sample sintered at 1400°C .

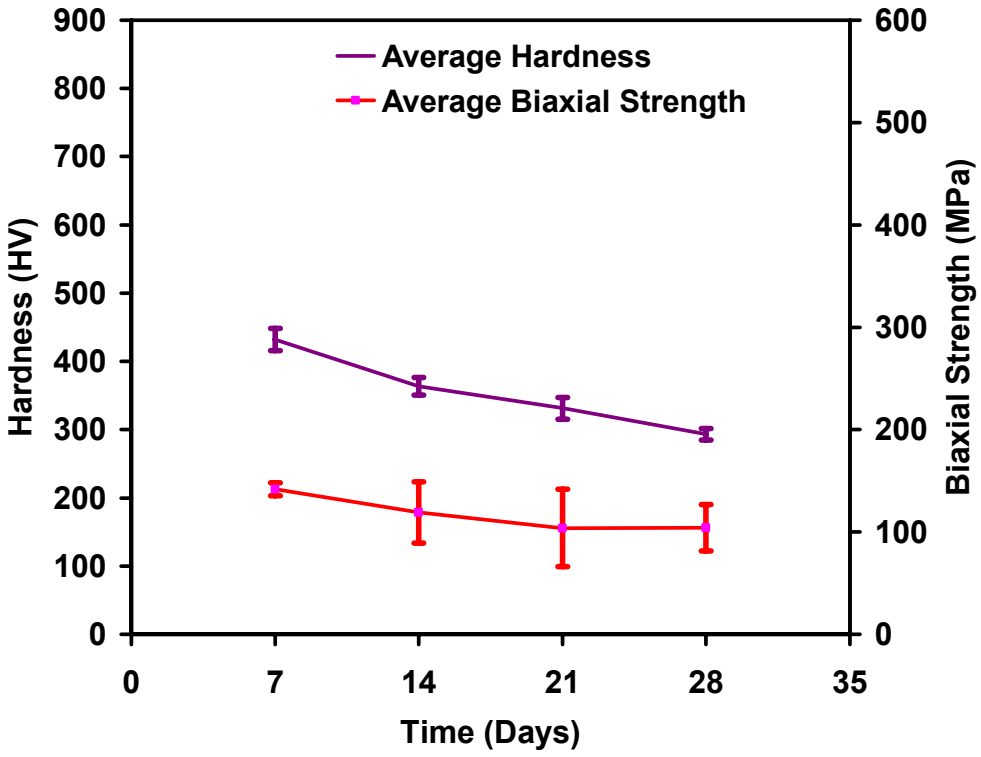

Figure 24: Variation of Hardness and Biaxial strength of sintered TiO_2 samples (1400^oC) in SBF.

4.4.3 Mass loss in TiO_2 and HAp samples

Loss in mass of sintered TiO_2 and HAp samples were observed in SBF with time. In case of HAp, increase in mass was observed in the 4th week. This may be due to the formation of apatite layer on the surface of HAp samples sintered at 1250^oC. At higher temperature, HAp decomposed into biphasic compound consisting of $NaCaPO_4$ and $Na_3Ca_6(PO_4)_5$.

According to Nikahira *et al.* [47] HAp samples containing $NaCaPO_4$ showed higher bioactivity than pure HAp [42]. $Na_3Ca_6(PO_4)_5$ is a new bioceramic whose bioactivity is much more than that of HAp [49].

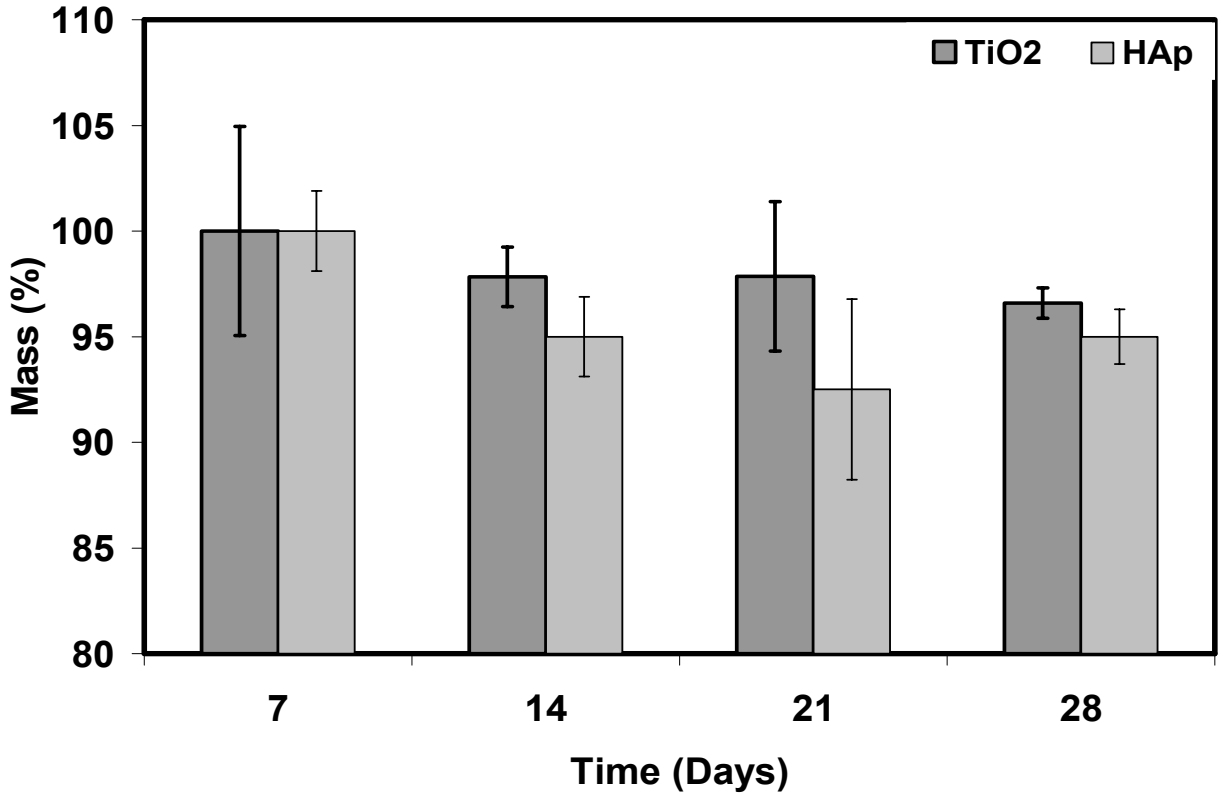

Figure 25: Loss in mass of TiO_2 sintered at 1400^{o}C and HAp sintered at 1250^{o}C in SBF,maintained in a dynamic state, as a function of time.

5. CONCLUSIONS

Microwave processing is an effective method to synthesize nanocrystalline HAp powder within short time. The technique is simple, economic, easy to repeat and can be optimized for mass production. Highly crystalline HAp powder with average particle size of 12 nm was achieved after microwave synthesis. TEM analysis confirmed the morphology of the powder as needle shaped with diameter of 5-10 nm and length of 15-30 nm. Calcination of the synthesized powder at 500^{o}C for 2 h increased average particle size to 21 nm. EDS confirmed elemental composition of the powder. FTIR analysis showed phase transformation after 1200^{o}C which became more prominent at 1250^{o}C. TG analysis showed 23% weight-loss upon heating up to 1200^{o}C, contributed by the removal of adsorbed & possible lattice water, decarboxylation of HAp or condensation of HPO_4^{2-} releasing water. We observed remarkably lower initial dehydroxylation temperature (570^{o}C) compared to reported values in literature for commercial hydroxyapatite (680^{o}C or higher).

In addition to HAp, β-$NaCaPO_4$ and $Na_3Ca_6(PO_4)_5$ were also observed at 950^{o}C, 1100^{o}C and 1200^{o}C. β-$NaCaPO_4$ and $Na_3Ca_6(PO_4)_5$ can be used to develop osteo-inductive or bio-resorbable calcium phosphate bioceramics because rate of bone growth on β-$NaCaPO_4$ and $Na_3Ca_6(PO_4)_5$ samples is much more than that of HAp. Bioactivity of $Na_3Ca_6(PO_4)_5$ new bioceramic is much better than that of HAp.

Density of HAp samples continued increasing with the increase in temperature from 1100^{o}C to 1250^{o}C and sintered density of 2.88 g/cc was obtained at 1250^{o}C.

Hardness and Biaxial strength of the HAp samples increased with temperature and maximum hardness value of 249.53 ± 3.98 HV and biaxial flexural strength of 52.07 ± 4.96 MPa were observed for samples sintered at 1250^{o}C.

Biaxial strength and hardness of TiO_2 samples increased with temperature. Maximum biaxial flexural strength of 125.5 ± 11.07 MPa and maximum hardness of 643.27 ± 7.96 HV were observed for the TiO_2 sample sintered at 1500^{o}C which was much more than that of sintered HAp samples.

Decrease in mass, hardness and biaxial strength of HAp samples sintered at 1250^{o}C and TiO_2 samples sintered at 1400^{o}C showed biodegradation in SBF, maintained in a dynamic state, as a function of time.

Increase in mass was observed for the HAp samples in SBF during the fourth week which may be due to fact that rate of apatite formation on the surface of HAp samples was more than the rate of dissolution of HAp samples. In case of TiO_2, no such phenomenon was observed.

6. FUTURE DIRECTIONS AND SUGGESIONS

Investigation is going on to achieve fine microstructure after sintering at high temperature. Conventional pressure-less sintering method requires long sintering time and results in coarse grain microstructure and low mechanical properties. Here I would like to use microwave radiation for sintering. Microwave sintering has been reported to produce fine microstructure with dense sintered HAp structure in a very short time [85]. Cracking of the samples can be avoided during sintering too.

Transformation of biphasic mixture of HAp and β -TCP at 1100^{o}C-1200^{o}C, into biphasic mixture of β-$NaCaPO_4$ and $Na_3Ca_6(PO_4)_5$ might expand the possibility of developing new calcium phosphate cement which is much more bioactive than HAp.

LIST OF REFERENCES

1. http://www.devicelink.com/news/100/2/27291.html

2. US Department of Health and Human Services, Bone Health and Osteoporosis a Report of the Surgeon General, US Dept of Health and Human Services, Public Health Service, Office of the Surgeon General, Rockville, MD (2004)

3. U.S.Market for Dental Implants and Dental Bone Substitutes December 2003,174 pages,Report#A335

4. www.mdi-md.com

5. Gleiter H., Prog. Mater. Sci., 33, (1989) 223

6. Ogiso M., J Biomed Mater Res Appl Biomater 1998: 43;318-20

7. Hench L.L., J Am Ceramic Society 1991: 74: 1487-510.

8. Mayo M.J., Nanostructured Materials: Science and Technology; Kluwer: Netherlands, 1998.

9. Karch J., Birringer R.; Gleiter H., Nature 330 (1987) 556-558.

10. Xu J.L., Khora K.A., Gub Y.W., Kumarb R., Cheang P., Biomaterials 26 (2005) 2197-207.

11. http://www.angstrommedica.com/images/FrostSullivan.htm

12. Paul W., Chandra C.P., Am. J. Biochem. & Biotechnol. 2 (2): 41-48, 2006.

13. Groot K.; Klein C.P.A.T.; Wolke J. G. C.; Blieck-Hogervorst J. M. A., Chemistry of Calcium Phosphate Bioceramics. In Handbook of Bioactive Ceramics, Vol. 2, Calcium Phosphate and Hydroxylapatite Ceramics, Yamamuro T.; Hench L. L.; Wilson J., Eds. CRC Press: Boca Raton, FL., 1990; pp 3-16.

14. Kalita S. J.; Bhardwaj A.; Bhatt H. A., Materials Science and Engineering: C 2007, 27, (3), 441.

15. http://www.geocities.com/ctas61/biomim.htm

16. http://www.imed.co.th/medical.htm

17. Heughebaert M., LeGeros R. Z., Gineste M., Guilhelm A., Bonel G., J. Biomed. Mater. Res. 1988, 22, (S14), 257-68.

18. Liu C., Huang Y., Shen W., Cui J., Biomaterials 22 (2001) 301–306.

19. Yang X., Wang Z., Mater J. Chem. 8 (1998) 2233–2237.
20. Feng W., Mu-sen L., Yu-peng L., Yong-xin Q., Mater. Lett. 59 (2005) 916–919.
21. Yen S.K., Lin C.M., Mater. Chem. Phys. 77 (2003) 70–76.
22. Itatani K., Nishioka T., Seike S., Howell F.S., Kishioka A., Kinoshita M., J. Am. Ceram. Soc. 77 (1994) 801–805.
23. Chen C.W., Riman R.E., TenHuisen K.S., Brown K., J. Cryst. Growth 270 (2004) 615–623.
24. Hui G.Z., Qingshan Z., Zhao H.X., Mater. Res. Bull. 40 (8) (2005) 1326–1334.
25. Suchanek W.L., Byrappa K., Shuk P., Riman R.E., Janas V.F., TenHuisen K.S., J. Solid State Chem. 177 (2004) 793–799.
26. Riman R.E., Suchanek W.L., Byrappa K., Chen C.W., Shuk P.I., C.S. Oakes, Solid State Ionics 151 (2002) 393–402.
27. Kuta P.M., Sfeir C., Lee D.-H, Olton D., Choi D., Acta Biomater. 1 (2005) 65–83.
28. Siddharthan A., Seshadri A.K. and Sampath Kumar T.S., Scripta Materialia 55 (2006) 175–178
29. Meejoo S.; Maneeprakorn W.; Winotai P., Thermochimica Acta 2006, 447, (1), 115-120.
30. Parhi P., Ramanan A., Ray A.R., Materials Letters 58 (2004) 3610-3612.
31. Han J., Song H., Saito F., Lee B., Materials Chemistry and Physics 99 (2006) 235-239.
32. Yang Z., Jiang Y., Wang Y., L. Ma, F. Li., Materials Letters 58 (2004) 3586-3590.
33. Jalota S., Bhaduri S.B., Tas A.C., J Biomed Mater Res Part B: Appl Biomater 80B: 304–316, 2007
34. Apel E., Holand W., Rheinberger V., US Pat. Appl. No. 2004/0167006 A1.
35. ICDD PDF No. 29–1193., The International Centre for Diffraction Data. Newtown Square, PA.
36. Kilian O., Wenisch S., Heiss C., Horas U., Dingeldein E., Schnettler R., Biomaterialien 2002;3:126– 132.
37. Tang R., Hass M., Wu W., Gulde S., Nancollas G.H.,. J Colloid Interface Sci 2003;260: 379–384.
38. Kwon S.H., Jun Y.K., Hong S.H., Kim H.E., J Eur Ceram Soc 2003;23:1039 –1045.

39. Knabe C., Berger G., Gildenhaar R., Howlett C.R., Markovic B., Zreiqat H. , Biomaterials 2004;25:335–344.

40. Ramselaar M.M.A, Driessens F.C.M., Kalk W, de Wijn JR, van Mullem P.J.. , J Mater Sci: Mater Med 1991;2:63–70.

41. Driessens F.C.M., Ramselaar M.M.A., Schaeken H.G., Stols A.L.H., van Mullem P.J. , J Mater Sci: Mater Med 1992;3:413– 417.

42. Ramselaar M.M.A., van Mullem P.J., Kalk W, de Wijn J.R., Stols A.L.H., Driessens F.C.M., J Mater Sci: Mater Med 1993;4:311–317.

43. Bermudez O., Boltong M.G., Driessens F.C.M., Ginebra M.P., Fernández E. and Planell J.A.. , Biomaterials 1994;15:1019 –1023.

44. Knabe C., Gildenhaar R., Berger G,, Ostapowicz W., Fitzner R., Radlanski R.J., Gross U. , J Biomed Mater Res 1993;27:1225–1233.

45. Kangasniemi, Groot K., Becht J.G.M., Yli-Urpo A.U., J Biomed Mater Res 1993;27:1225–1233

46. Doi Y., Shimizu Y., Moriwaki Y., Aga M., Iwanaga H., Shibutani T., Yamamoto K., Iwayama Y., Biomaterials 22 (2001) 847-854.

47. Nakahira A., Konishi S., Nishimura F., Iwasaka M., Ueno S., J Appl Phys 2003;93:8513–8515.

48. Gong W., Abdelouas A., Lutze W., J Biomed Mater Res 2001;54:320 –327.

49. TMS 2008 Symposium: Biological Materials Science, Abstract: Synthesis and Characterization of Sodium Calcium Phosphate for Biological Applications, Authors: Hande Demirkiran, Pranesh B. Aswath

50. Yeong K.C.B., Wang J., Ng S.C., Materials Letters 38 (1999) 208.

51. Royer A., VIguie J.C., Heughebrert M., Journal of Materials Science. Materials in Medicine 4 (1993) 76

52. Best S., Bonfield W., J. Mater. Sci., Mater. Med. 5 (1994) 516-21

53. Webster T.J., Ergun C., Doremus R.A., Siegel R.A. and Bizios R., Biomaterials 21 (2000) 1803.

54. Ruys A.J., Wei M., Sorrell C.C., Dickson M.R., Brandwood A., Milthorpe B.K., Biomaterials 16 (1995) 409–415.

55. Muralithan G., Ramesh S., Int. 26 (2000) 221–230.

56. Correia R.N., Magalhaes M.C.F., Marques P.A.A.P., Senos A.M.R., J. Mater. Sci. Mater. Med. 7 (1996) 501–505.

57. Itokazu M., Yang W., Aoki T., Ohara A., Kato N., Biomaterials 19 (1998) 817-819.

58. Bauer T.W., Geesink R.G.T., Zimmerman R., Mcmohan J.T., J Bone Joint Surg (Am) 73 (1991) 1439-1452.

59. Tas A.C., Biomaterials 21 (2000) 1429-1438.

60. Lopes M.A., Santos J., Monteiro F.J., Knowles J.C., J Biomed Mater Res, 39 (1998) 244–251.

61. Knowles J.C., Ceramic Industry Division Annual Convention, Brunel University, 20-23 April 1993.

62. Wei J., Journal of Material Science, 38(2003), 3303-3306

63. Fanga L., Gaob P., Lenga Y.., Composite: Part B 38 (2007) 345-351.

64. Ji B.H, Gao H.J, J Mech Phys Solids 2004: 52 (9) :1963-90.

65. Liao S., Wang W.,UO M., Ohkawaa S., Akasaka T., Tamura K., Cuib F., Watari F., Biomaterials 26(2005) 7564-7571.

66. Fu Q., Zhou N., Huang W., Wang D., Zhang L., Li H., DOI: 10. 1002/ jbm.a. 30322

67. Xu F.L., Li Y.B., Yao X.M., Wang X.J., Acta Mater. Comp. Sinica 22 (1) (2005) 27.

68. Lin R., Mao X., Yu Q., Tan B., Current Applied Physics, 7S1 (2007) e85-89.

69. Furuzono T., Walsh D., Sato K., J Artif Organs (2004) 7:137-144.

70. Zhu S.H., Huang B.Y., Zhou K.C., Journal of Nanoparticle Research, 6: 307-311. 2004

71. Diebold U., Surf. Sci. Rep., 48, (2003) 53.

72. Somnath C., Roy A.B., Maggie P., Craig A.G., Biomaterials 28 (2007) 4667-4672.

73. Kuhn K.P., Chaberny I.F., Massholder K., Stickler M., Benz V.W., Sonntag H., Erdinge L., Chemosphere 53 (2003) 71-77.

74. Mills A., Chemical Society, Rev.22(1993) 417.

75. Martin P.M., Monzyk B.F., Burckle E.C., Busch J.C., Gilbert R.J., Dasse K.A., Materials Science and Engineering B 119 (2005) 246–251

76. Suryanarayana C. and Norton M.G., X-Ray Diffraction: A Practical Approach. Plenum Press: New York, 1998.

77. Kokubo T., Takadama H., Biomaterials 27 (2006) 2907–2915

78. Wang, T., Dorner-Reisel A., Muller E., J Europ Ceram Soc 2004, 24, 693-98.

79. Cihlao J., Buchal A.; Trunce M., J Mater Sci 1999, 34, 6121-31.

80. Hartmann, P., Jager C., Barth S., Vogel J., Meyer K., Journal of Solid State Chemistry 2001, 160, (2), 460-68.

81. Gross K. A.., Berndt C. C., Stephens P., Dinnebier R., Journal of Materials Science 1998, 33, (15), 3985-91.

82. Manjubala I., Sivakumar M., Materials Chemistry and Physics 71 (2001) 272–278.

83. Pattanayak D.K., Dash R., Prasad R.C., Rao B.T., Rama Mohan T.R., Materials Science and Engineering C 27 (2007) 684–690

84. Ito A., Nakamura S., Aoki H., Akao M., Teraoka K., Tsutsumi S., Onuma K., Tateishi T., Journal of Crystal Growth 163 (1996) 311 - 317

85. Ramesh S.A., Tan C.Y., Bhaduri S.B., Teng W.D., Ceramics International 33 (2007) 1363–1367

86. Rameshbabu N., Prasad Rao K., Sampath Kumar T.S., Journal of Material Science 40-(2005) 6319-6323.

87. Siddharthan A., Seshadri S.K. and Sampath Kumar T.S., Trends Biomater. Artif. Organs, Vol 18 (2), January 2005.

88. Nithyanantham T., Kandasamy C., Gnanama F.D., Ceramics International 28 (2002) 355–362.